ARL-TR-9076 ● SEP 2020

DEVCOM ARMY RESEARCH LABORATORY

Polar Format Algorithm for 3-D Imaging with Forward-Looking Synthetic Aperture Radar

by Traian Dogaru

Approved for public release; distribution is unlimited.

NOTICES

Disclaimers

The findings in this report are not to be construed as an official Department of the Army position unless so designated by other authorized documents.

Citation of manufacturer's or trade names does not constitute an official endorsement or approval of the use thereof.

Destroy this report when it is no longer needed. Do not return it to the originator.

ARL-TR-9076 ● SEP 2020

Polar Format Algorithm for 3-D Imaging with Forward-Looking Synthetic Aperture Radar

by Traian Dogaru
Sensors and Electron Devices Directorate, CCDC Army Research Laboratory

Approved for public release; distribution is unlimited.

REPORT DOCUMENTATION PAGE

Form Approved
OMB No. 0704-0188

Public reporting burden for this collection of information is estimated to average 1 hour per response, including the time for reviewing instructions, searching existing data sources, gathering and maintaining the data needed, and completing and reviewing the collection information. Send comments regarding this burden estimate or any other aspect of this collection of information, including suggestions for reducing the burden, to Department of Defense, Washington Headquarters Services, Directorate for Information Operations and Reports (0704-0188), 1215 Jefferson Davis Highway, Suite 1204, Arlington, VA 22202-4302. Respondents should be aware that notwithstanding any other provision of law, no person shall be subject to any penalty for failing to comply with a collection of information if it does not display a currently valid OMB control number.
PLEASE DO NOT RETURN YOUR FORM TO THE ABOVE ADDRESS.

1. REPORT DATE *(DD-MM-YYYY)*	2. REPORT TYPE	3. DATES COVERED (From - To)
September 2020	Technical Report	April–July 2020

4. TITLE AND SUBTITLE
Polar Format Algorithm for 3-D Imaging with Forward-Looking Synthetic Aperture Radar

5a. CONTRACT NUMBER

5b. GRANT NUMBER

5c. PROGRAM ELEMENT NUMBER

6. AUTHOR(S)
Traian Dogaru

5d. PROJECT NUMBER

5e. TASK NUMBER

5f. WORK UNIT NUMBER

7. PERFORMING ORGANIZATION NAME(S) AND ADDRESS(ES)
CCDC Army Research Laboratory
ATTN: FCDD-RLS-RU
Adelphi, MD 20783-1138

8. PERFORMING ORGANIZATION REPORT NUMBER
ARL-TR-9076

9. SPONSORING/MONITORING AGENCY NAME(S) AND ADDRESS(ES)

10. SPONSOR/MONITOR'S ACRONYM(S)

11. SPONSOR/MONITOR'S REPORT NUMBER(S)

12. DISTRIBUTION/AVAILABILITY STATEMENT
Approved for public release; distribution is unlimited.

13. SUPPLEMENTARY NOTES
ORCID ID: Traian Dogaru, 0000-0002-1091-4928

14. ABSTRACT

This report investigates the application of the polar format algorithm (PFA) to 3-D image formation using the forward-looking synthetic aperture radar system proposed by the US Army Combat Capabilities Development Command Army Research Laboratory with the goal to assist helicopter landing in degraded visual environments. The basic PFA is developed for this unusual radar sensing geometry, emphasizing some differences from the traditional side-looking SAR configuration. Several implementation details are discussed, such as sampling requirements, data interpolation, and the algorithm extension to multistatic antenna array. We then develop a procedure for wavefront curvature error correction (WCEC), starting with a thorough analysis of these phase errors and ending with a description of the WCEC algorithm implementation. At each stage along the way, we illustrate the theory with numerical examples.

15. SUBJECT TERMS
synthetic aperture radar, forward-looking radar, radar imaging, polar format algorithm, degraded visual environment

16. SECURITY CLASSIFICATION OF:			17. LIMITATION OF ABSTRACT	18. NUMBER OF PAGES	19a. NAME OF RESPONSIBLE PERSON
a. REPORT	b. ABSTRACT	c. THIS PAGE			Traian Dogaru
Unclassified	Unclassified	Unclassified	UU	71	19b. TELEPHONE NUMBER (Include area code) (301) 394-1482

Standard Form 298 (Rev. 8/98)
Prescribed by ANSI Std. Z39.18

Contents

List of Figures

List of Tables

1. Introduction

The US Army Combat Capabilities Development Command (CCDC) Army Research Laboratory (ARL) is currently working on the development of a millimeter-wave (MMW) forward-looking synthetic aperture radar (FLSAR) to assist helicopter landing in degraded visual environments (DVE). This program supports the Future Vertical Lift cross functional team, which represents one of Army's modernization priorities. Specifically, CCDC Army Research Laboratory is proposing a low cost, size, weight, and power MMW radar system that combines a linear antenna array and aircraft motion to obtain high-resolution 3-D imagery of an area of interest (e.g., the potential landing zone). This information would be passed to the pilot via helmet-mounted display to assist in deciding whether the landing zone is safe.

An initial study of this radar system[1] established the baseline performance metrics, including resolution, grating lobes, timing, power, and sensitivity to motion errors, indicating the possible levers available to the system designer and their associated tradeoffs. Since then, several additional papers investigating various aspects of the ARL DVE FLSAR have been published.[2–4] In all this previous work, the image formation process was handled by the backprojection algorithm (BPA), in either time- or frequency-domain implementation (note the frequency-domain implementation has been called the "matched filter method" in some of our previous work; the two algorithms are equivalent).

While the BPA is considered the "golden standard" in radar imaging due to its accuracy and flexibility, other synthetic aperture radar (SAR) algorithms with superior computational efficiency may be more suitable for imaging applications requiring real-time operation, such as the radar system for landing-zone mapping in DVE conditions. In this report we investigate the applicability of the polar format algorithm (PFA) to this radar configuration.

The PFA is a mature image formation procedure that has been known within the SAR community for several decades.[5,6] The core of this algorithm consists of a multidimensional fast Fourier transform (FFT) from the sampled radar data to the image domain, which is far more efficient than the computations required by the BPA. Nevertheless, the major shortcoming of the PFA is the fact that it relies on the plane wave approximation of the radar wave propagation, which is the same as assuming the radar and the image domain are placed in the far field region with respect to one another. When this assumption becomes invalid, the algorithm introduces errors in the image due to a propagation phenomenon known as wavefront curvature. A significant body of work[5–8] has been dedicated to the

wavefront curvature error correction (WCEC) in the context of PFA to extend the algorithm's applicability to more-general synthetic aperture geometries.

In this study, we adapt the PFA to the specific FLSAR geometry, showing that this geometry requires a different formulation of the algorithm than the traditional side-looking SAR configuration. Furthermore, we perform a detailed analysis of the phase errors introduced by the wavefront curvature and present a new approach to the WCEC that is entirely different from previous studies in this area. Additionally, we adapt the PFA to the implementation of multistatic antenna arrays, which is an essential part of the FLSAR system design. All these steps in the algorithm development are illustrated with numerical examples representing the imaging system's point spread function (PSF), with point targets placed at various locations throughout the image domain.

The report is organized as follows. Section 2 describes the FLSAR system geometry and reviews several possible imaging algorithms for this application, including a detailed presentation of the PFA. In Section 3, we show numerical examples of images obtained by the PFA and discuss implementation details such as data interpolation and sampling requirements, as well as the algorithm extension for multistatic antenna arrays. Section 4, dedicated to the WCEC, starts with an analysis of the phase errors, then develops the new WCEC procedure for the FLSAR images. We draw this study's conclusions in Section 5.

2. System Description and Imaging Algorithms

2.1 FLSAR System Description

The principle of the helicopter-mounted FLSAR system for 3-D landing-zone imaging can be explained in reference to Fig. 1, which describes all the relevant parameters of the sensing geometry. Thus, the system is equipped with a 2-m-wide front-bumper-type linear antenna array that provides resolution in the azimuth direction (dictated by the integration angle $\Delta\phi$), while the forward motion of the platform at constant height creates a synthetic aperture with sufficient elevation look-angle diversity $\Delta\theta$ to offer resolution in the vertical direction. The radar waveform bandwidth (0.5–1 GHz) provides resolution in the third direction (downrange). Further details on the proposed system, including typical operational parameters, waveforms, timing, antenna array configurations, and other design aspects can be found in our previous work.[1]

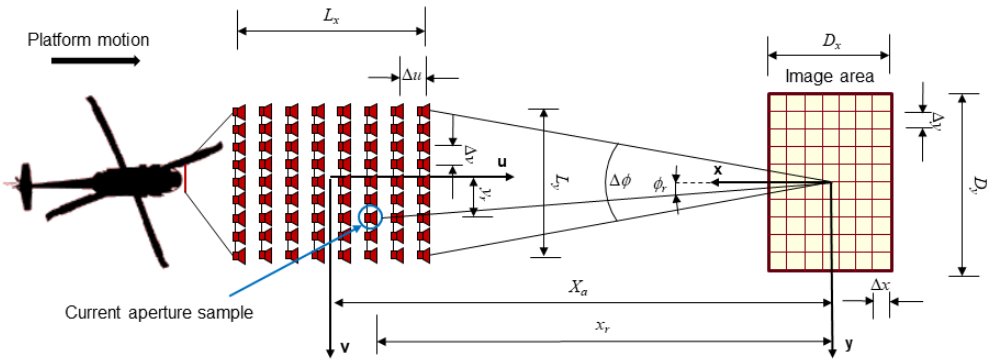

(a)

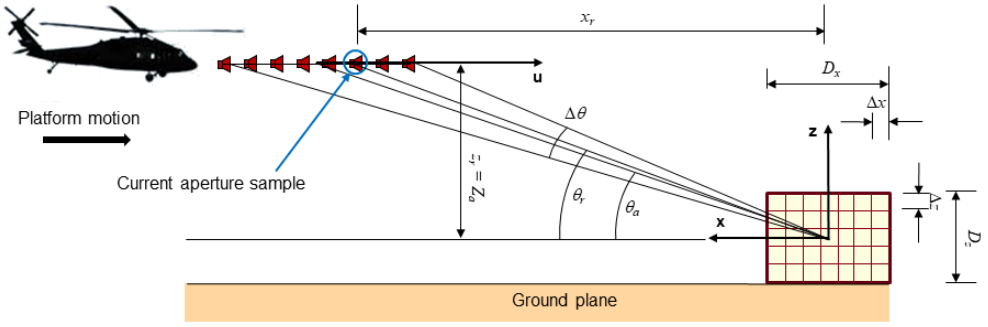

(b)

Fig. 1 Schematic representation of the helicopter-borne radar system operating as FLSAR, showing the relevant sensing geometry from a) top view and b) side view. The small antenna diagrams mark the aperture sample positions. (Drawing not to scale.)

The Cartesian coordinate system (x, y, z) has the origin in the image center, with D_x, D_y, and D_z denoting the image extents in the three directions. The aperture samples used in image formation are obtained from the antenna array elements (in the y direction) and the forward synthetic aperture positions (in the x direction) and are placed in a uniform, rectangular 2-D array with overall dimensions L_y and L_x, respectively. We introduce the separate coordinates u and v, with the origin in the middle of the 2-D sample array, to characterize the sample positions within the 2-D aperture. The middle of the 2-D aperture has the Cartesian coordinates $(X_a, 0, Z_a)$ with respect to the image center, and $R_a = \sqrt{X_a^2 + Z_a^2}$ is the range between the aperture center and the image center. One difference from the geometry described in our previous report consists of moving the origin of the z axis to $\frac{D_z}{2}$ above the ground plane; this choice was made to simplify the subsequent derivation of the PFA.

Throughout this section, we consider a monostatic SAR system, meaning the radar transmitter (Tx) and receiver (Rx) are collocated for each aperture sample. The changes to the imaging algorithms required by a more realistic multistatic antenna array geometry were partially discussed in previous work.[1] As a follow-up, we examine the impact of considering a multistatic system on the PFA formulation in Section 3.5 of this report.

We assume the radar data are available in the frequency domain, at L frequency samples f_l, as if the radar system operated with stepped-frequency waveforms. Upon down-conversion, the expression of the frequency domain point target response (PTR) of a target placed at coordinates (x_0, y_0, z_0), with the radar antenna at (x_r, y_r, z_r), and at frequency f_l is

$$\mathrm{PTR} = \exp\left(-jk_{R,l}\sqrt{(x_r - x_0)^2 + (y_r - y_0)^2 + (z_r - z_0)^2}\right), \tag{1}$$

where $k_{R,l} = \dfrac{4\pi f_l}{c}$ (the subscript R stands for "radial"). In this expression, we ignored any magnitude variation of the radar signal with the target and radar aperture sample positions.

Note that stepped-frequency waveforms are not necessarily a commonly used solution for practical MMW radar systems; however, they are entirely appropriate for our FLSAR model and have the advantage of simplifying some derivations. A much more common implementation of SAR systems employs linear frequency modulated (LFM), or chirp waveforms; the vast majority of textbooks and publications related to SAR theory start the analysis with these types of waveforms.[5–8] Moreover, the preferred method for compressing LFM waveforms consists of stretch processing,[9] where the received signal is mixed (or "de-ramped") with a replica of the transmitted signal, rescaled from time to frequency samples, and finally Fourier-transformed to obtain the range profile characterizing a given radar location along the synthetic aperture. Our frequency domain SAR signal model is equivalent to considering the LFM waveforms after the de-ramping and rescaling steps but before the final Fourier transform performed in stretch processing. Specific issues related to this processing technique, such as the residual video phase[5] (RVP), are discussed in most textbooks and are simply ignored in this work.

When we consider the radar received signals, we initially set their phase origin at the radar antenna location. Again, this is not always a faithful representation of the way radar signals are processed in a practical system but serves the purpose of our

model. In fact, different SAR imaging algorithms have their own requirements in choosing the phase origin of the radar signals, and the phase adjustments required by each specific algorithm are indicated as part of the algorithm descriptions.

2.2 Backprojection Algorithm

The BPA and its variants has been employed in the vast majority of the SAR imaging work performed at ARL for over two decades. BPA represents a brute force, direct implementation of the exact matched filter for the SAR system geometry, in either frequency-aperture dimensions (the "frequency domain BPA") or fast time-aperture dimensions (the "time domain BPA") of the radar data.[9,10]

To formulate the BPA, it is easiest to start with its frequency domain implementation—this has been called the "matched filter method" in some of our previous SAR imaging work.[1] We assume the radar collects data from *M* different monostatic locations (or aperture samples) placed in an arbitrary geometrical pattern in the 3-D space. Let $S_m(f_l)$ be the signal received at aperture sample index *m* and frequency index *l*, and (x, y, z) the current image voxel coordinates. Then the complex amplitude of the current voxel is computed as

$$I(x,y,z) = \frac{1}{LM}\sum_{l=1}^{L}\sum_{m=1}^{M} S_m(f_l)\exp\left(jk_{R,l}R_m\right), \tag{2}$$

where $R_m = \sqrt{\left(x_{r,m}-x\right)^2 + \left(y_{r,m}-y\right)^2 + \left(z_{r,m}-z\right)^2}$.

In Eq. 2, f_l is the frequency of the passband signal, all coordinates are referenced to the Cartesian system origin (placed in the center of the image), and the $S_m(f_l)$ signal phase is referenced to the radar antenna location.

Although the matched filter in the frequency domain version of the BPA achieves exact compensation of the radar signal phase when the current voxel coincides with the target location, this algorithm is very inefficient from a computational standpoint. Thus, the operations in Eq. 2, consisting of a double sum over all frequency and aperture samples, must be repeated for all voxels in the image. Moreover, the algorithm does not take advantage of any FFT type of computations, which constitute the foundation of the vast majority of efficient algorithms in radar signal processing.

An improvement in the execution speed of the BPA can be obtained if the radar data are first converted from frequency to time domain via inverse FFTs. One important detail in this operation is that to achieve an alias-free conversion via FFT

with a reasonable number of frequency samples, the phase origin of the radar signal must be shifted from the radar antenna location to the Cartesian system origin in the image center. This phase adjustment can be written as

$$S_m^0\left(f_l\right) = S_m\left(f_l\right)\exp\left(jk_{R,l}\sqrt{x_{r,m}^2 + y_{r,m}^2 + z_{r,m}^2}\right) = S_m\left(f_l\right)\exp\left(jk_{R,l}r_{r,m}\right). \quad (3)$$

After this operation, which performs a passband-to-baseband conversion in the range dimension, the radar signal's Nyquist sampling rate in frequency is dictated solely by the image depth (or downrange swath), which is typically much smaller than the radar–voxel range. Let $s_m^0\left(t\right)$ be the time domain version of $S_m^0\left(f\right)$ obtained via FFT. Since the frequency-to-time domain FFT acts only on the baseband part of the signal spectrum, the complex $s_m^0\left(t\right)$ signal contains a residual phase factor corresponding to the carrier frequency. With these provisions, the time domain version of the BPA is described by the following equation:

$$I\left(x,y,z\right) = \sum_{m=1}^{M} s_m^0\left(\frac{2R_m^0}{c}\right)\exp\left(jk_{R0}R_m^0\right), \quad (4)$$

where $k_{R0} = \dfrac{4\pi f_0}{c}$ corresponds to the carrier frequency f_0, and

$$R_m^0 = R_m - r_{r,m} = \sqrt{\left(x_{r,m}-x\right)^2 + \left(y_{r,m}-y\right)^2 + \left(z_{r,m}-z\right)^2} - \sqrt{x_{r,m}^2 + y_{r,m}^2 + z_{r,m}^2}\,. \quad (5)$$

Note the factor $\exp\left(jk_{R0}R_m^0\right)$ that compensates for the residual carrier frequency phase factor previously mentioned. Since the waveforms $s_m^0\left(t\right)$ are sampled at discrete times, the delay $\tau_m = \dfrac{2R_m^0}{c}$ computed for a particular aperture-position-voxel pair usually does not coincide with one of those time samples. To avoid computationally costly on-the-fly interpolations, a common procedure is to oversample the original waveforms by a large factor (at least 32) with respect to the time domain Nyquist rate and select the sample corresponding to τ_m from the new waveform based on the nearest neighbor rule. Tapered windows are typically applied to the frequency domain data $S_m\left(f_l\right)$ in both frequency and aperture dimensions for image sidelobe reduction.

As noted in Eq. 4, the time domain BPA involves a single sum (over aperture samples) for each image voxel computation, which represents an improvement over the frequency domain version. A detailed analysis of the computational complexity of these algorithms is beyond the scope of this report. Nevertheless, neither BPA

version takes advantage of FFT-type processing; this shortcoming has prompted the SAR community to develop more computationally efficient image formation algorithms, such as the range migration algorithm (RMA) and PFA.

2.3 Range Migration Algorithm

The RMA represents the current state of the art in Fourier-based SAR image formation algorithms, combining an accuracy comparable to BPA with the computational advantages provided by employing multidimensional FFT operations.[5,10] A complete derivation of the RMA is clearly beyond the scope of this study. In the following, we simply list the steps involved in the RMA implementation for the FLSAR system:

- Start with the frequency domain samples $S_m\left(f_l\right)$, with the phase referenced to the radar antenna position, as discussed in Section 2.1.
- Oversample the data in the frequency dimension and zero-pad the data in the *y* (azimuth) direction. The reasons for these operations are discussed further in this section. Apply tapered windows in the frequency and aperture dimensions for sidelobe control.
- Convert the data to baseband in the k_u dimension (the Fourier counterpart of the forward aperture coordinate *u*). This consists of multiplying the data by the factor $\exp\left(jk_{R0}\cos\theta_a u\right)$, where θ_a is the grazing angle from the middle of the 2-D aperture to the Cartesian system origin. Note this operation is specific to squinted aperture geometries.
- Take a 2-D inverse FFT of the new data along the two aperture dimensions (*u* and *v*). At this point, the radar data lie in a 3-D space of coordinates k_R, k_u, and k_v. Note that these coordinates represent passband versions of the corresponding *k*-domain variables.
- Multiply the data in this domain by the factor $\exp\left(j\sqrt{k_R^2-k_u^2-k_v^2}Z_a+jk_uX_a\right)$. This operation implements a "coarse matched filter" and has the role of performing passband to baseband conversions in the *z* dimension (the first phase term) and the *u* dimension (the second phase term), respectively. Note the second phase term in the exponential factor is again specific to squinted aperture geometries.
- Perform the Stolt interpolation. This is a 1-D interpolation from the k_R variable samples to uniformly spaced samples in $k_z=\sqrt{k_R^2-k_u^2-k_v^2}$. At the same time, relabel k_u as k_x and k_v as k_y (a coordinate order permutation is

associated with the coordinate relabeling in the FLSAR configuration). At this point, the data lie in a 3-D space of coordinates k_x, k_y, k_z, which are the Fourier counterparts of the image domain coordinates x, y, z.

- Take a 3-D FFT of the interpolated data set to obtain the image in the spatial domain.

Implementing RMA for the FLSAR system presents some major challenges due to the severely squinted forward aperture geometry (the squint angle is typically 80° for this system). For this reason, we were not able to find many publications discussing the application of RMA to FLSAR imaging systems in the literature. A lone paper by Soumekh[11] proposed a forward-looking radar imaging system based on RMA (interestingly, the application was also related to guided aircraft landing), although its principle was somewhat different from the ARL-proposed FLSAR system. The main challenges encountered in this RMA implementation can be summarized as follows:

- The RMA involves back and forth FFTs between the y and k_y variables (the initial transformation is in fact between v and k_v, which are equivalent to y and k_y). When we perform these FFTs, we must make sure the data are sampled at or above the Nyquist rates in both y and k_y variables to avoid aliasing. For the FLSAR geometry, the image cross-range is much larger than the aperture length in azimuth ($D_y >> L_y$). The aperture sampling rate in y must satisfy $\Delta y \le \frac{\lambda_0 R_a}{2D_y}$, as discussed in our previous work. However, to satisfy the Nyquist sampling rate in k_y, we require $\Delta k_y \le \frac{2\pi}{D_y}$. Since we have $\Delta k_y = \frac{2\pi}{L_y^{ds}}$, where L_y^{ds} is the aperture data support for the initial $y \to k_y$ FFT, we infer that $L_y^{ds} \ge D_y$. In other words, the azimuth aperture data support must be at least as large as the cross-range image dimension. Since the actual aperture size L_y is much shorter than D_y (typically by a factor of 10), the former needs to be extended by zero-padding the original azimuth aperture data to match the image size in cross-range. This requirement increases the total number of radar data samples in the azimuth dimension by a large multiple.

- During the Stolt interpolation from k_R to k_z variables, the grid representing the radar sample locations in the k-domain incurs a rotation by the squint angle $90^o - \theta_a$ in the k_x-k_z plane (as previously mentioned, this angle is large, around 80°). If the sample spacing in k_R is Δk_R, the sample spacing in k_z is

$\Delta k_z = \frac{\Delta k_R}{\sin\theta_a} = \frac{4\pi\Delta f}{c\sin\theta_a}$. At the same time, the required Nyquist rate for k_z sampling is $\Delta k_z = \frac{2\pi}{D_z}$; from here we derive $\Delta f = \frac{c\sin\theta_a}{2D_z}$. (Note: to be exact, θ_a should be replaced by θ_{min}, the smallest possible radar–voxel angle in the entire FLSAR configuration). This result matches the one derived by Soumekh.[10] The presence of the $\sin\theta_a$ factor in the numerator means that the sampling rate in frequency required by the RMA is significantly larger than that required by the BPA (typically by a factor of 6). Additionally, note that the frequency sampling rate for RMA depends on the vertical image dimension D_z, whereas the same sampling rate for BPA depends on D_x.

The FLSAR-specific requirements of zero-padding the aperture in azimuth and oversampling the signals in frequency bring the total number of radar samples to process by RMA to an unacceptably large figure and eventually negate this algorithm's computational advantages. Indeed, a comparison of the computational complexity between RMA and the time domain BPA applied to the FLSAR system, for the same radar data set and image size, shows that the two methods involve similar numbers of floating-point operations. Although we successfully implemented the RMA for the FLSAR system, the algorithm's rather underwhelming computational performance in this application made us abandon it and continue the search for faster imaging methods.

2.4 Polar Format Algorithm

The PFA was a relatively early development within the SAR community[12] and has been subsequently replaced by the more advanced RMA in most applications. The latter algorithm achieves a similar computational efficiency for conventional SAR geometries, without relying on the approximations specific to PFA. However, there are still specific sensing scenarios, such as the FLSAR system investigated by ARL, where the PFA is not affected by the same challenges as the RMA (described in Section 2.3). The main goal of this report is to show that when coupled with the WCEC procedure, PFA can produce accurate imaging results for this radar system with far better computational efficiency than both RMA and BPA.

The main tenet of the PFA is that the SAR received signal obtained at one frequency and one aperture location represents a sample in the *k*-domain characterizing the reflectivity of the entire scene under investigation. Since the *k*-domain represents the Fourier counterpart of the spatial image domain, the image (more exactly, the spatial reflectivity map) can be obtained by a 2-D or 3-D Fourier transform of the radar data. Note this methodology is different from the more precise RMA

approach, where the radar signal obtained from the entire scattering scene, at one frequency and aperture location, covers an extended area (or volume) in the *k*-domain. RMA requires additional processing in this domain to reduce these scene responses to single *k*-domain samples, which are subsequently converted to the image domain by Fourier transform.

The validity of the PFA approach relies on the plane wave approximation of the radar wave propagation, which assumes the radar and target scene are placed in the far-field region with respect to one another. As previously discussed, the far-field assumption is not satisfied for our FLSAR geometry, meaning that the PFA-formed images will exhibit errors caused by the wavefront curvature phenomenon.[5] In this section we formulate the basic PFA for the FLSAR configuration. In Section 3 we present numerical examples of images obtained by the basic PFA, demonstrating the errors introduced by this procedure. In Section 4 we perform a detailed analysis of these phase errors and develop a method to correct them.

To establish the 3-D PFA formulation for the FLSAR system, we start from Eq. 2 (describing the exact matched filter for the SAR image) and use the following approximation of the radar–voxel range:

$$\begin{aligned} R &= \sqrt{\left(x_r - x\right)^2 + \left(y_r - y\right)^2 + \left(z_r - z\right)^2} \cong \sqrt{x_r^2 + y_r^2 + z_r^2} - \frac{xx_r + yy_r + zz_r}{\sqrt{x_r^2 + y_r^2 + z_r^2}} \\ &= r_r - \frac{xx_r + yy_r + zz_r}{r_r} = r_r - \left(x\cos\phi_r\cos\theta_r + y\sin\phi_r\cos\theta_r + z\sin\theta_r\right) \end{aligned} . \quad (6)$$

Note the subscript *r* stands for the radar location coordinates (including the angular coordinates ϕ and θ), and, as compared with the formulas in Section 2.2, we dropped the index *m* representing the aperture sample. The approximation in Eq. 6 assumes that the image dimensions are much smaller than the radar range r_r. When plugged into the PTR formula, we obtain

$$\mathrm{PTR} = \exp\left(-jk_R R\right) \cong \exp\left[-jk_R\left(r_r - \left(x\cos\phi_r\cos\theta_r + y\sin\phi_r\cos\theta_r + z\sin\theta_r\right)\right)\right]. \quad (7)$$

Aside from the factor $\exp\left(-jk_R r_r\right)$, which depends on the radar location only, the remaining phase factor $\exp\left[jk_R\left(x\cos\phi_r\cos\theta_r + y\sin\phi_r\cos\theta_r + z\sin\theta_r\right)\right]$ represents a plane wave propagating at angles ϕ_r and θ_r with wavenumber $k_R = \frac{4\pi f}{c}$. According to the principle of stationary phase (PSP),[5,9] the angles characterizing a radar signal sample in the *k*-domain are the same as the line-of-sight propagation angles in the physical space. Consequently, these three

coordinates (k_R, ϕ_r, θ_r) are sufficient to completely characterize the wave vector **k**, or the radar sample's location in the *k*-domain. In the following, we drop the subscript *r* from the angles ϕ and θ, since these angles are always referenced in relation to the radar sample location.

In PFA, the radar signal at frequency index *l* and aperture location index *m*, $S_m(f_l)$, undergoes the same phase adjustment as indicated by Eq. 3, which consists of multiplication by the factor $\exp\left(jk_{R,l}r_{r,m}\right)$. Note that since we assume that the radar coordinates with respect to the Cartesian system origin (or the image center) are known at each aperture sample location, this phase adjustment can be performed as a computational step within the algorithm. However, more often this operation is implemented directly in the radar receiver hardware, by introducing the appropriate time delay in the mixing signal used in de-ramping or down-conversion.[5] The resulting phase-adjusted PTR can be written as

$$\mathrm{PTR}^0 = \exp\left[jk_R\left(x\cos\phi\cos\theta + y\sin\phi\cos\theta + z\sin\theta\right)\right]. \qquad (8)$$

We denote the phase-adjusted radar signal received from a general target scene by $S^0(k_R, \phi, \theta)$: This shows that the signal depends on frequency (via k_R) and aperture position (via ϕ and θ). The image reconstruction procedure consists of applying a matched filter with transfer function given by the conjugate of the expression in Eq. 8 to the signal $S^0(k_R, \phi, \theta)$:

$$\begin{aligned} I(x,y,z) &= \sum_{k_R}\sum_{\phi}\sum_{\theta} S^0(k_R,\phi,\theta)\exp\left[-jk_R\left(x\cos\phi\cos\theta + y\sin\phi\cos\theta + z\sin\theta\right)\right] \\ &= \sum_{k_x}\sum_{k_y}\sum_{k_z} S^0(k_x,k_y,k_z)\exp\left[-j\left(k_x x + k_y y + k_z z\right)\right] \end{aligned} \quad , \qquad (9)$$

where $k_x = k_R\cos\phi\cos\theta$, $k_y = k_R\sin\phi\cos\theta$ and $k_z = k_R\sin\theta$. The sums are computed over the available samples in the corresponding variables. Now it becomes clear that the image reconstruction procedure described by Eq. 9 resembles a discrete version of a 3-D Fourier transform from the *k*-domain variables (k_x, k_y, k_z) to the image domain variables (x, y, z).

To enable the implementation of this Fourier transform by a 3-D FFT, we need to ensure the data samples in the *k*-domain are arranged in a rectangular and uniformly spaced grid in the (k_x, k_y, k_z) variables. Since the original radar data samples are not typically collected in a pattern that satisfies this condition, the data must be

interpolated from the original (k_R, ϕ, θ) sample grid to the FFT-ready grid in the (k_x, k_y, k_z) coordinates.

Traditionally, the PFA has been developed for 2-D side-looking SAR geometries, where the radar data samples form a polar pattern in the *k*-domain; the interpolation is then performed from a polar to a rectangular grid in this domain, hence the "polar format" name of the algorithm. However, the radar samples in the forward-looking geometry of the ARL-proposed system do not conform to this polar pattern, as seen in the plots in Fig. 2. Additionally, the forward aperture samples do not form a uniformly spaced grid in the θ angle. Consequently, we found it more useful to work with the radar sample coordinates (k_R, v, u) instead of (k_R, ϕ, θ). This approach has the advantage that the original radar samples are uniformly spaced when expressed as a function of the (k_R, v, u) coordinates; this sample uniformity would not hold when working with the (k_R, ϕ, θ) coordinates.

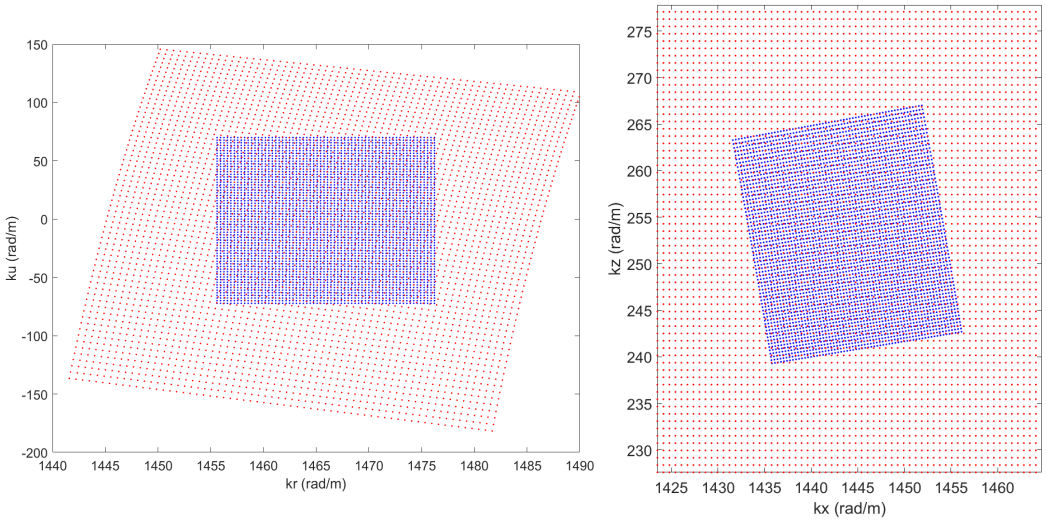

(a) (b)

Fig. 2 Positions of the radar data samples (blue dots) and image samples (red dots) in the k-domain as a function of a) k_R and k_u variables and b) k_x and k_z variables. The image samples exhibit a wider k-domain coverage than the radar data samples because the image pixels are oversampled by a factor of 2 with respect to the resolution cell size. Note in this graphic representation, the k-domain samples are down-sampled by a factor of 16 in all dimensions.

Note we have $x_r = X_a - u$, $y_r = v$, and $z_r = Z_a$, and we can establish the following transformations between the (k_R, v, u) and (k_x, k_y, k_z) sets of coordinates:

$$k_x = k_R \frac{X_a - u}{\sqrt{(X_a - u)^2 + v^2 + Z_a^2}} \qquad k_R = \sqrt{k_x^2 + k_y^2 + k_z^2}$$

$$k_y = k_R \frac{v}{\sqrt{(X_a - u)^2 + v^2 + Z_a^2}} \qquad u = X_a - Z_a \frac{k_x}{k_z} \quad . \quad (10)$$

$$k_z = k_R \frac{Z_a}{\sqrt{(X_a - u)^2 + v^2 + Z_a^2}} \qquad v = Z_a \frac{k_y}{k_z}$$

As an alternative to the aperture coordinates u and v, we can use the variables $k_u = u\frac{k_{R0}}{R_a}$ and $k_v = v\frac{k_{R0}}{R_a}$, which have the same physical dimension as k_x, k_y, k_z, and k_R. (Note: k_u and k_v are not the Fourier counterparts of u and v, but simply scaled-up version of these variables.) In fact, the radar and image sample positions in Fig. 2a are represented as a function of the k_u and k_R coordinates.

When using the (k_R, v, u) set of coordinates, the reconstruction procedure becomes

$$I(x,y,z) = \sum_{k_R} \sum_{u} \sum_{v} S^0(k_R, v, u) \exp\left(-jk_R \frac{x(X_a - u) + yv + zZ_a}{\sqrt{(X_a - u)^2 + v^2 + Z_a^2}} \right). \quad (11)$$

The application of the PFA to the FLSAR geometry involves a 3-D interpolation from the (k_R, k_v, k_u) coordinates, characterizing the radar data, to the (k_x, k_y, k_z) coordinates, characterizing the k-domain image data. Details related to the data sampling and interpolation in the k-domain are discussed in Sections 3.3 and 3.4.

To summarize, the PFA implementation for the FLSAR system involves the following processing steps:

- Start with the frequency domain samples $S(f, v, u)$, with the phase referenced to the radar antenna positions, as discussed in Section 2.1.
- Apply tapered windows in the frequency and aperture dimensions for sidelobe control.
- Perform the phase adjustment of these samples by the factor $\exp(jk_R r_r)$ to obtain the new data samples $S^0(k_R, k_v, k_u)$.
- Interpolate these samples from the original data grid of (k_R, k_v, k_u) coordinates to a rectangular, uniformly spaced grid of (k_x, k_y, k_z) coordinates.

- Take a 3-D FFT of the interpolated data set to obtain the image in the spatial domain.

All three algorithms presented in this section (BPA, RMA, and PFA) result in images with the same nominal resolution in the three Cartesian directions[1]:

$$\delta x = \frac{c}{2B\cos\theta_a}, \tag{12a}$$

$$\delta y = \frac{\lambda_0 R_a}{2L_y}, \tag{12b}$$

$$\delta z = \frac{\lambda_0 R_a}{2L_x \tan\theta_a}. \tag{12c}$$

In Eq. 12a, B is the radar signal bandwidth. Note these resolution formulas assume no tapered windows are applied in the frequency and aperture dimensions. When we introduce those windows, the resolution cell size increases by a typical factor between 1.5 and 1.8.

In the case of PFA, because of the wavefront curvature errors issue, only the voxel at the image center (placed in the Cartesian system origin) is perfectly focused with the resolution given by Eq. 12. Voxels placed away from the image center exhibit some varying degree of defocusing, meaning these resolution formulas do not apply in those cases. However, after performing the WCEC procedure presented in Section 4, the voxel resolution is restored to its nominal values in Eq. 12.

3. PFA Imaging Examples and Implementation Details

3.1 2-D Images Obtained by PFA

In this section, we demonstrate numerical examples of 2-D images obtained by PFA, illustrating the two aperture configurations that together make up the 3-D FLSAR geometry: the side-looking aperture (in the *x*-*y* plane) and the forward-looking aperture (in the *x*-*z* plane). In the side-looking aperture configuration we only consider monostatic radar samples along the physical aperture direction (*y* axis) placed at fixed *x* and *z* coordinates. In the forward-looking aperture configuration, we use radar samples along the forward synthetic aperture direction (*x* axis) while keeping the *y* and *z* coordinates fixed. The SAR system parameters used in these examples are exaggerated (as compared with the practical ARL-proposed FLSAR system) with the purpose of creating very large sized images, which offer a clear illustration of the wavefront curvature errors issue. Investigating

the 2-D imaging geometries separately has the advantages of reasonable execution times (for large images) and simplicity of graphic representation. The full 3-D FLSAR configuration, applied to an image size better aligned with this project's objectives, is demonstrated in Section 3.2.

For both aperture configurations, we chose a horizontal radar range of 1000 m and size-up the other parameters to achieve the FLSAR system's nominal spatial resolution of 0.25–0.3 m. For this purpose, we need to ensure the aperture sizes provide integration angles in azimuth and elevation of 0.8°–1° independent of the radar range. At 1000-m range, this results in aperture sizes (in both x and y directions) much larger than the practical FLSAR system proposed by ARL, which is designed to achieve the nominal resolution at 150–200-m range. The resulting SAR images shown in this section contain 1024 pixels in all three Cartesian directions. The following is a complete list of the system parameters used for 2-D imaging by PFA:

- Carrier frequency f_c = 35 GHz
- Bandwidth B = 500 MHz, from 34.7–35.2 GHz
- Fixed aperture width L_y = 14 m
- Synthetic aperture length L_x = 100 m
- Radar platform height Z_a = 175 m
- Average horizontal range X_a = 1000 m; horizontal range varies from 1050 to 950 m
- Number of samples in frequency = 1024, spaced 0.49 MHz apart
- Number of samples along fixed azimuth aperture (y direction) = 1024, spaced 1.37 cm apart
- Number of samples along forward-looking aperture (x direction) = 1024, spaced 0.1 m apart

The resulting angular parameters are

- Azimuth integration angle: $\Delta\phi$ = 0.8°, varying in 0.0008° steps
- Elevation integration angle: $\Delta\theta$ = 1°, varying in 0.001° steps
- Average slant angle: θ_a = 10°, varying from 9.4° to 10.4° across the aperture

The image sizes are 156 × 156 m (for the side-looking aperture) and 156 × 128 m (for the forward-looking aperture), respectively; in both cases, we use 1024 pixels in all directions. This results in a pixel size of 15.2 cm in x and y directions and

12.5 cm in the z direction. Note the pixel size is chosen approximately half of the resolution cell size to avoid the so-called "straddling losses", which are typical to FFT-based radar imaging systems and may induce unpredictable magnitude fluctuations of the image pixels. Additionally, we use Hamming windows in all three radar data dimensions (frequency, y- and x-directed apertures) to suppress the image sidelobes. Due to the presence of these windows, the half-width of the PSF mainlobe (or effective image resolution) spans approximately three image pixels. Further details on the data and image sampling requirements for this algorithm are discussed in Section 3.3.

The scattering scenes to be mapped in both configurations are made of eight point targets placed at various location throughout the image. Figure 3 plots the image obtained for side-looking configuration (x-y plane), while Fig. 4 shows the image obtained for forward-looking configuration (x-z plane). The true target coordinates are listed in Table 1. Note we used different sets of target coordinates between the side-looking and forward-looking cases.

In all SAR images throughout this report, the radar is placed on the right side of the page, which is opposite from the diagram in Fig. 1. The pixel/voxel magnitudes are represented in decibels, with a dynamic range of 40 dB.

As previously discussed, the PFA images are afflicted by the wavefront curvature phase errors. One effect of these errors is to induce shifts in the image coordinates with respect to the true target coordinates. The dependence of these spatial shifts on the imaging system parameters and target locations is fairly complex and is analyzed separately in Section 4.1. Generally, the shifts are larger as the targets are placed further away from the image center. Table 1 indicates the location of target images obtained by the uncorrected PFA as compared with the true target locations for the 2-D imaging examples.

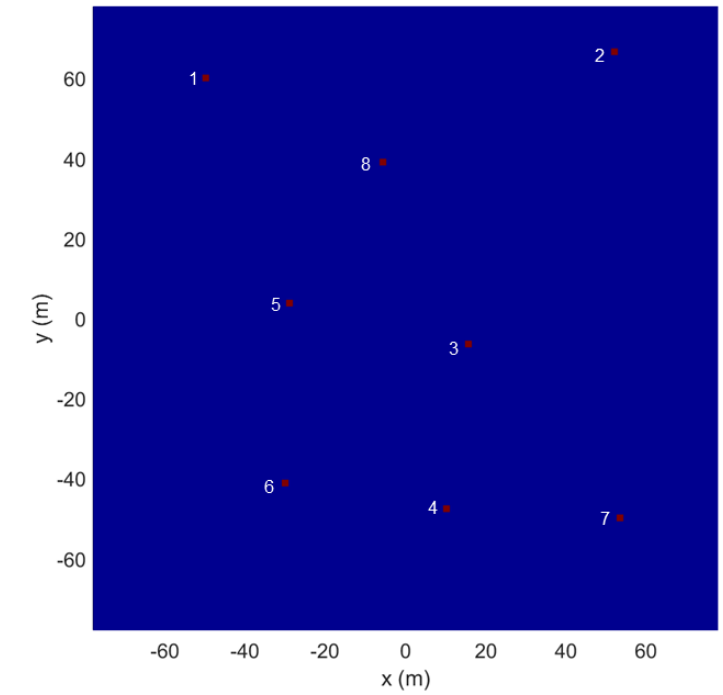

(a)

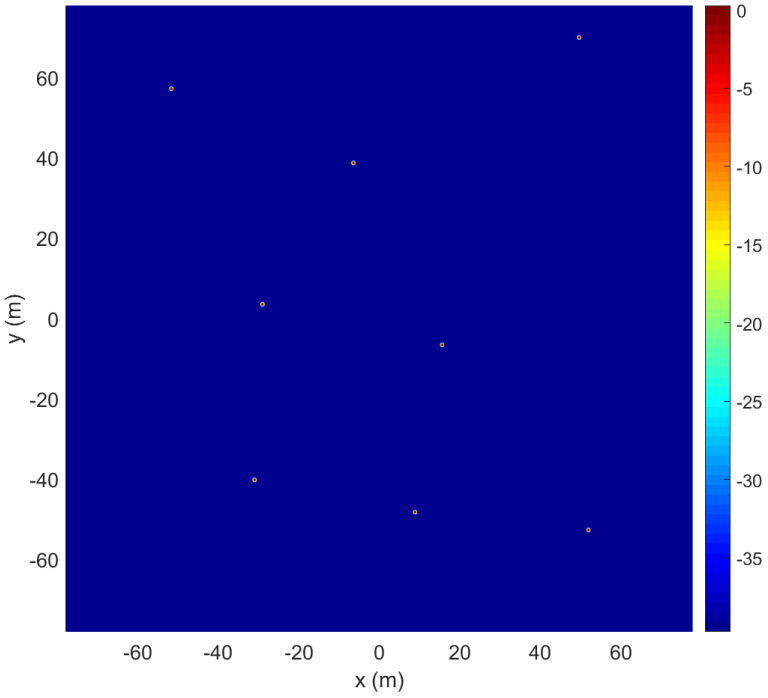

(b)

Fig. 3 2-D SAR image obtained for the side-looking geometry in the x-y plane, showing a) true locations of the point targets (red squares on blue background) and b) SAR image of these targets obtained by PFA. The target numbers are indicated in Fig. 3a.

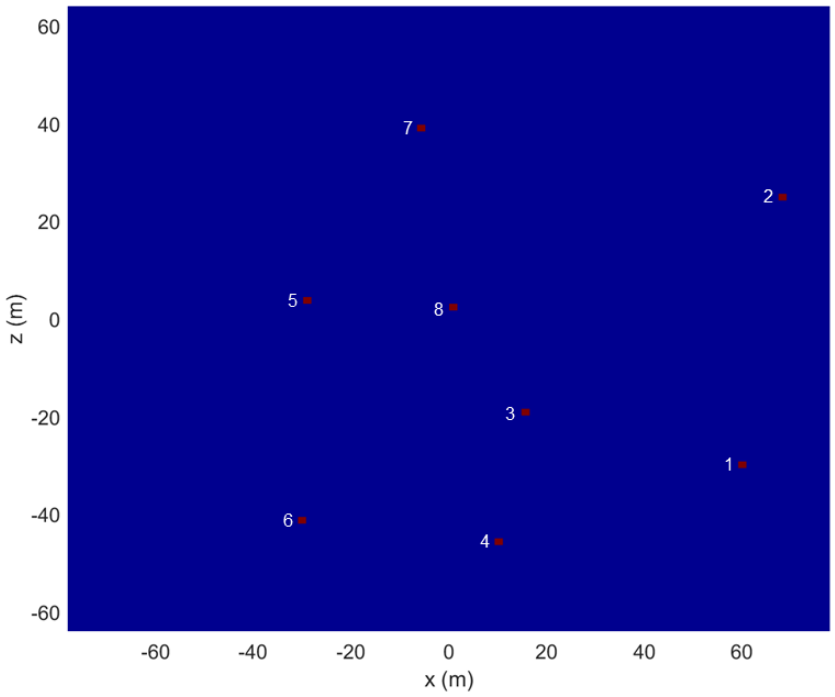

(a)

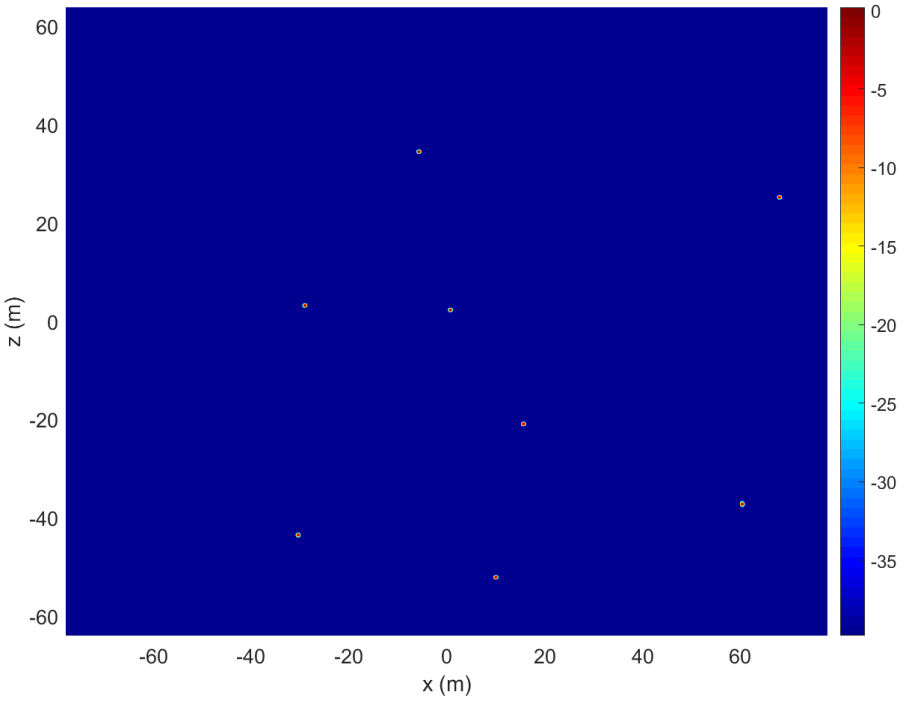

(b)

Fig. 4 2-D SAR image obtained for the forward-looking geometry in the x-z plane, showing a) true locations of the point targets (red squares on blue background) and b) SAR image of these targets obtained by PFA. The target numbers are indicated in Fig. 4a.

Table 1 Target coordinates in the 2-D side-looking and forward-looking SAR configurations, showing the true locations as well as their images obtained by direct application of the PFA

Target number	Side-looking				Forward-looking			
	True		PFA		True		PFA	
	x (m)	y (m)	x (m)	y (m)	x (m)	z (m)	x (m)	z (m)
1	–50.0	60.0	–51.8	57.1	60.0	–30.0	60.4	–37.3
2	52.0	66.5	49.6	69.9	68.2	24.8	68.1	25.2
3	15.6	–6.5	15.5	–6.6	15.6	–19.3	15.7	–20.9
4	10.0	–47.8	8.9	–48.2	10.0	–45.8	10.0	–52.1
5	–29.1	3.6	–9.1	3.5	–29.1	3.6	–29.1	3.2
6	–30.2	–41.4	–31.1	–40.2	–30.2	–1.4	–30.4	–43.5
7	53.3	–50.0	52.0	–52.7	–5.7	38.9	–5.8	34.5
8	–5.7	38.9	–6.6	38.7	0.7	2.3	0.7	2.3

One possible simplification of the PFA for SAR systems operating with narrowband waveforms and narrow-angle aperture integration—with aperture at broadside—relies on the fact that in that scenario the radar measurement samples form a pattern very close to a rectangular, uniform grid in the *k*-domain. In that case, a direct 2-D FFT of the radar data (with the appropriate scaling of the axes) can yield the image in the spatial domain without the need for any sample interpolation from the radar measurement to Cartesian coordinates in the *k*-domain. This procedure should apparently work for the side-looking aperture considered in this section, which satisfies all the conditions enumerated. Nevertheless, we found by numerical experiments that skipping the interpolation step in PFA, even for this well-behaved imaging scenario, leads to serious image distortions, especially when the targets are located far from the image center. The image distortions in the absence of *k*-domain sample interpolation are even more severe in the case of the forward-looking aperture, which presents a very large squint angle as compared with the side-looking counterpart. The main reason for this effect is the strong nonlinear relationship between the k_z and u variables (see Eq. 10), which precludes the application of a simple linear mapping from the radar measurement to Cartesian coordinates in the *k*-domain. Consequently, every time we have applied the PFA to 2-D or 3-D imaging throughout this report, we performed the *k*-domain sample interpolation across all available radar signal dimensions.

3.2 3-D Images Obtained by PFA

The extension from the 2-D imaging geometries in Section 3.1 to the full 3-D geometry of the FLSAR system is straightforward. The 3-D imaging by PFA was

described in Section 2.4. As part of this procedure, a 3-D data interpolation is performed from the radar measurement sample coordinates (k_R, k_v, k_u) to the image k-domain Cartesian coordinates (k_x, k_y, k_z).

In the 3-D case, the radar system and image parameters are chosen to match the desired performance metrics of the proposed FLSAR system for helicopter landing assistance. Note that as compared with the parameters in Section 3.1, the radar range is only 200 m, the physical aperture (antenna array) has a length of 2 m, and the image size is limited to 20 × 20 × 16 m. The resulting sensing geometry achieves the following nominal image resolution: 0.3 m in the x direction, 0.4 m in the y direction, and 0.33 m in the z direction, respectively. The complete list of radar system parameters follows:

- Carrier frequency f_c = 35 GHz
- Bandwidth B = 500 MHz, from 34.7 to 35.2 GHz
- Fixed aperture width L_y = 2 m
- Synthetic aperture length L_x = 15 m
- Radar platform height Z_a = 34 m
- Average horizontal range X_a = 200 m; horizontal range varies from 192.5 to 207.5 m
- Number of samples in frequency = 128, spaced 3.9 MHz apart
- Number of samples along fixed azimuth aperture (y direction) = 128, spaced 1.56 cm apart
- Number of samples along forward-looking aperture (x direction) = 128, spaced 0.117 m apart
- Azimuth integration angle: $\Delta\phi$ = 0.6°, varying in 0.0047° steps
- Elevation integration angle: $\Delta\theta$ = 0.75°, varying in 0.006° steps
- Average slant angle: θ_a = 10°, varying from 9.6° to 10.4° across the aperture

We use four point targets placed at coordinate sets listed in Table 2 together with the coordinates of their image peaks. These targets are not connected in any way with those considered in the 2-D cases from Section 3.1. In the 3-D case, the number of voxels in the three Cartesian directions are 128 × 128 × 128, respectively, with a voxel size of 15.6 cm in the x and y dimensions and 12.5 cm in the z dimension. We again apply Hamming windows to the radar data in all dimensions. This results

in an effective image resolution cell size extending over approximately three voxels in each direction. Since the graphic representation of the 3-D images is somewhat difficult, Fig. 5 only displays four vertical planar cuts in the *y*-*z* plane corresponding to the *x* coordinate of each target image peak. Note that these peaks can only be determined with an accuracy comparable to the voxel size. As in the 2-D cases, the largest target coordinate shifts occur in the *z* direction.

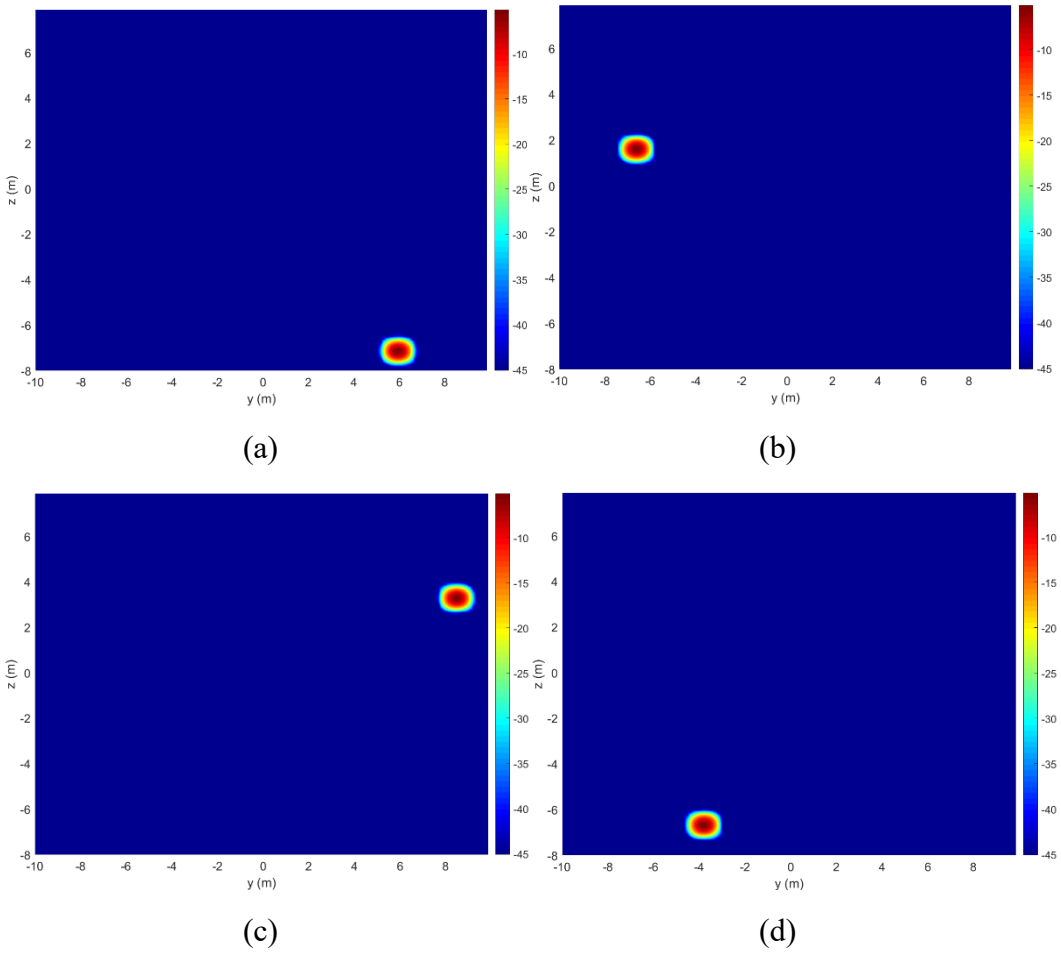

Fig. 5 Vertical y-z planar cuts through the 3-D PFA image obtained for the full FLSAR configuration at x coordinates corresponding to the four target image peaks: a) x = –8.125 m (Target 3), b) x = –5.937 m (Target 4), c) x = 5.937 m (Target 1), and d) x = 6.719 m (Target 2)

Table 2 Target coordinates in the 3-D FLSAR configurations, showing the true locations as well as their images obtained by direct application of the PFA

Target number	True			PFA		
	x (m)	y (m)	z (m)	x (m)	y (m)	z (m)
1	5.9	8.2	4.4	5.9	8.5	3.3
2	6.7	–3.7	–5.6	6.7	–3.8	–6.7
3	–8.1	6.2	–6.5	–8.1	5.9	–7.1
4	–5.9	–6.8	2.5	–5.9	–6.6	1.6

3.3 Sampling Requirements for Radar Data and Image Domains

In this section, we discuss criteria for setting the sampling rates of the radar data and image voxels in all relevant dimensions. In terms of radar data sampling, the major consideration is avoiding target aliasing in images with the desired spatial extent. The image voxel size is typically chosen in relation to the resolution cell size, such that all possible image details are captured by its graphic representation.

Before we establish precise criteria for sampling rate setting, we need to mention the fact that FFT-based algorithms do not allow independent selection of the sample spacing between the two corresponding Fourier variables. For example, if we consider the frequency and range as the Fourier variable pair, the choice of a frequency step Δf and a total number of samples N uniquely determines the range sample spacing resulting from FFT processing, $\Delta R = \frac{c}{2N\Delta f}$. Apparently, this mathematical identity prohibits the simultaneous arbitrary choice of both Δf and ΔR. Note this issue is not relevant to imaging algorithms that do not make use of FFT processing, such as those belonging to the BPA family.

Nevertheless, independent selection of sampling rates in both radar data and image voxels is still possible in PFA due to the presence of the intermediary interpolation step between the two data sets. Thus, the sampling rates in frequency and aperture dimensions (u and v) are dictated by the Nyquist criterion based on the image overall extent, as explained shortly. On the other hand, the image voxel size dictates the data coverage in the k-domain (or $\left(k_x, k_y, k_z\right)$ variables) before the final 3-D FFT step of the PFA. The 3-D interpolation from the $\left(k_R, v, u\right)$ to the $\left(k_x, k_y, k_z\right)$ variables has the role to reconcile the mismatch between the two coordinate grids, whose sample locations do not coincide regardless of how we pick the image voxels and radar data sampling intervals.

The Nyquist rate requirements for radar data sampling established in our previous work[1] for the BPA are equally valid for the PFA. These are the following:

$$\Delta f = \frac{c}{2D_x \cos\theta_a} \tag{13a}$$

$$\Delta v = \frac{\lambda_0 R_a}{2D_y} \tag{13b}$$

$$\Delta u = \frac{\lambda_0 R_a}{2D_z \tan\theta_a} \tag{13c}$$

These sampling rates ensure that any point target placed throughout the image does not introduce grating lobes within the image extent. However, satisfying these conditions does not guarantee that targets located outside the image frame do not create grating lobes within that domain. There are two main methods to suppress the grating lobes induced by out-of-image-frame targets:

1) Use radar antennas with beam patterns that approximately match the image extent in azimuth and elevation dimensions (note that this method cannot be applied to the downrange dimension). This way, returns from targets outside the image domain are "filtered out" by the antenna pattern. Because these patterns do not have an abrupt angular cutoff, some grating lobe leakage resulting from out-of-image strong targets is always a possibility. Therefore, the system designers cannot solely rely on this method for grating lobe suppression.

2) Use a digital spatial filter in the radar data domain that rejects returns from targets outside the image domain. This procedure is called "spotlighting" by Soumekh.[10] In the context of PFA, this filtering operation can be easily implemented based on the approximate 3-D Fourier relationship between the radar data and image. For this processing to work, the original radar data must be oversampled with respect to the rates indicated by Eq. 13. We propose an oversampling factor of 2, meaning the procedure can handle grating lobes from targets placed anywhere within twice the actual image extent. Any targets placed outside these dimensions should be handled by the antenna pattern filter.

The grating lobe suppression digital spatial filter is implemented as a preprocessing operation via the following steps:

- Start with the radar data sampled at half the intervals given by Eq. 13 (that means an oversampling factor of 2). For instance, in the 2-D side-looking example in Section 3.1, the frequency Nyquist rate computed by Eq. 13a is

0.98 MHz. However, in the actual simulation, we doubled up the sampling rate by setting the sampling interval to 0.49 MHz.

- Take a 3-D FFT of those data to obtain an approximate version of the radar image. Note that since this image formation procedure skips the 3-D *k*-domain data interpolation step, this approximate radar image may contain some severe distortions. However, we expect that target positions in this image do not deviate too far from their true locations.
- Apply a 3-D filter in the image domain with the transfer function:

$$H\left(f_f, f_v, f_u\right) = \begin{cases} 1 \text{ for } f_f \in \left[-\dfrac{D_x \cos\theta_a}{c}, \dfrac{D_x \cos\theta_a}{c}\right] \\ \qquad \text{and } f_v \in \left[-\dfrac{D_y}{\lambda_0 R_a}, \dfrac{D_y}{\lambda_0 R_a}\right] \\ \qquad \text{and } f_u \in \left[-\dfrac{D_z \tan\theta_a}{\lambda_0 R_a}, \dfrac{D_z \tan\theta_a}{\lambda_0 R_a}\right] \\ 0 \text{ otherwise} \end{cases} . \qquad (14)$$

  In this equation, $\left(f_f, f_v, f_u\right)$ are the Fourier counterparts of $\left(f, v, u\right)$ and correspond loosely to scaled versions of the image coordinates $\left(x, y, z\right)$. This procedure filters out the targets placed outside the desired image extent while keeping the inside targets untouched.
- Take a 3-D inverse FFT from the image domain back to the radar data domain and restart the PFA procedure with the new data set.

Note the spotlighting procedure described by Soumekh[10] is more complex because it takes into account the quadratic terms describing the phase variation as a function of the aperture coordinates. However, for the narrowband and narrow-angle aperture characterizing the MMW FLSAR system, these quadratic terms can be neglected during the filtering procedure. In practice, we found the digital filtering procedure indicated in this section to offer satisfactory results in our application, with very little additional computational burden to the image formation process. If needed, certain margins can be added to the image extent to account for the shifts incurred by the target images due to the wavefront curvature error issue.

This grating lobe suppression method can be applied to FLSAR imaging as a preprocessing step regardless of the actual algorithm employed in image formation (including BPA). The only price we must pay to achieve this suppression is the oversampling of the radar data. While this is typically not a significant issue in the

frequency and synthetic aperture dimensions, it may impose a rather difficult design requirement on the antenna array, where the addition of extra elements can be major factors in raising the system's cost and complexity. Techniques for reducing the number of antenna elements using multistatic array configurations are discussed in Section 3.5. After the application of the grating lobe suppression digital filter, the radar data can be down-sampled back to the Nyquist rates given by Eq. 13 to reduce the computational burden on the imaging algorithm. However, as we show in Section 3.4, the 3-D interpolation procedure specific to the PFA directly benefits from using the oversampled radar data; consequently, the data are left unchanged after the spatial filtering operation.

Regarding the choice of the sampling interval in the image domain (or the voxel size), an obvious choice is to make it no larger than the image resolution cell size, such that one captures all the features available in the radar map obtained at that resolution level. However, setting the voxel size exactly equal to the resolution cell size is not a good practical solution, particularly in FFT-based radar signal processing schemes, due to the straddling loss issue.[13] In a nutshell, the straddling loss occurs when the radar signal's peak does not align with the middle of a resolution cell obtained at the output of the FFT operation. As a result, the image magnitude can exhibit unpredictable fluctuations (of up to 6 dB) that are not directly related to the target's scattering strength. A good rule of thumb that mitigates this issue is to pick the pixel or voxel size of the radar image as half the nominal resolution cell size.

Additionally, using tapered windows across the radar data dimensions (with the primary purpose of suppressing the image sidelobes) has a positive effect on reducing the straddling losses. In all our imaging examples throughout this report, the pixel or voxel size is set to about half of the nominal resolution cell size given by Eq. 12 and to about one-third of the effective resolution cell size obtained after data windowing. Note these image sampling issues and mitigation solutions are not only specific to PFA, but apply to all other SAR imaging algorithms.

3.4 Data Interpolation and Computational Complexity

The radar data interpolation from the (k_R, k_v, k_u) coordinates to the (k_x, k_y, k_z) coordinates is a crucial step in PFA. As discussed in Section 3.1, for the FLSAR system, the interpolation must be performed in all three data dimensions to obtain good imaging results. The interpolation can be performed in the (k_R, k_v, k_u) space or in the (k_x, k_y, k_z) space. In the first case, one computes the positions of the image samples in terms of the (k_R, k_v, k_u) variables; the resulting interpolation process

takes place from a uniform grid (radar data samples) to a nonuniform grid (image samples). In the second case, one computes the positions of the radar data samples in terms of the $\left(k_x, k_y, k_z\right)$ variables; the resulting interpolation process is performed from a nonuniform grid (radar data samples) to a uniform grid (image samples).

Traditionally, the data interpolation in PFA has been recast as a resampling procedure and implemented via the so-called polyphase filters.[5,6] The resampling procedure that changes the data sampling rate by a factor $L = \frac{M}{N}$ (with M and N integers) is discussed in numerous texts[14,15] and is not repeated here. In one dimension, this filtering operation can be described by the following equation:

$$s_{out}\left(m\right) = \sum_{n=-P}^{P} s_{in}\left(n\right) h\left(mM - nN\right), \tag{15}$$

where $h\left(k\right) = \text{sinc}\left(\frac{k}{N}\right)$ is the filter's impulse response and $2P+1$ is the filter's order.

Note for a 3-D imaging configuration, the 1-D filter must be applied three times across the entire data set, one dimension at a time, to obtain the effect of a full 3-D data interpolation. The typical resampling filters have finite impulse response (FIR) and must satisfy the following conditions[14]: 1) have a zero-phase transfer function, 2) behave as low-pass filters with the digital cutoff frequency $f_c = \frac{1}{2\max\left(M, N\right)}$, and 3) $h\left(0\right) = 1$ and $h\left(n\right) = 0$ for $n = \pm kN$, with k integer.

Since either the input or output data samples in the interpolation process are unevenly spaced, the polyphase filters are typically designed by setting N as large as needed such that the nonuniform sample grid can be closely fitted to points of coordinates $\frac{m}{N}$, with m integer. By this procedure, only one filter is required for the entire 1-D data sequence.

We attempted to implement this interpolation procedure using the MATLAB[16] function *resample*, which performs a 1-D resampling procedure that takes a nonuniform sample grid as input and produces a uniform sample grid as output (which means it must operate in one of the $\left(k_x, k_y, k_z\right)$ variables). Unfortunately, the resulting code was slow and generated a significant amount of artifacts in the output image. The main reason why this procedure is computationally inefficient is

the very large filter length (reaching up to 2000 coefficients in some cases) resulting from the need to accommodate the highly nonuniform data samples characterizing the FLSAR system geometry. The cause of the image artifacts is not entirely clear at this point, but one explanation could be the fact that the interpolation is performed one dimension at a time instead of globally on the 3-D radar data.

Instead of continuing the implementation efforts via the polyphase filters, we tried an entirely different approach to the data interpolation step, based on cubic spline functions. Although this was an ad hoc solution motivated primarily by the efficient MATLAB implementation of the *interp3* function (performing 3-D interpolation), this procedure turned out both accurate and fast from a computational standpoint.

Computational details of the cubic spline interpolation are described in textbooks[17] and are not included in this report. Note the cubic spline interpolation represents a completely different data processing methodology than the resampling by polyphase filters. If regarded as an FIR filter, the cubic spline interpolation coefficients satisfy the three conditions previously enumerated. However, these FIR filters have very low order (compared with the high-order polyphase filters) and their coefficients are data-dependent (unlike the polyphase counterpart). Despite the empirical evidence showing that cubic splines can be successfully employed in the PFA, we do not claim any optimality of this choice for the interpolation method. Further investigation efforts may reveal more-efficient and more-accurate techniques to replace this approach in the PFA implementation.

In general, the low-pass FIR filters equivalent to any interpolation method cannot exhibit the ideal transfer function with a perfectly abrupt cutoff. In this respect, there is a classic tradeoff between the filter length (which relates to the computational efficiency) and the filter's roll-off characteristic in the transition region (which relates to the interpolation accuracy).[15] The FIR interpolation filter departure from an ideal low-pass transfer function means that some amount of signal aliasing can occur in the process. This issue is particularly relevant to the case of the low-order spline interpolation filters. A simple method to ensure a margin against this aliasing is to oversample the original signal beyond the Nyquist rate. Note this scheme meshes perfectly with the radar data oversampling requirement for the spatial anti-aliasing filter implementation discussed in Section 3.3. In practice, we found that using data oversampled by a factor of 2 as an input to the cubic-spline interpolation procedure is sufficient to avoid any visible aliasing in the final SAR image created by PFA.

So far we have not commented on the overall computational complexity of the PFA. The algorithm stage that should apparently dominate the execution time is the 3-D FFT from the k-domain to the image domain. If N_x, N_y, and N_z are the numbers of

voxels in the three Cartesian directions, the number of operations required by this 3-D FFT is on the order of $N_x N_y N_z \log_2\left(N_x N_y N_z\right)$. Note this number can be orders of magnitude smaller than the number of operations required by the core of the time-domain BPA, on the order of $N_x N_y^2 N_z^2$ (here, we assumed that the *x* direction corresponds to downrange, as in Fig. 1).

Nevertheless, this simplistic comparison of the two algorithms does not take into account some significant amount of overhead involved in both algorithms. In the case of the PFA, it turns out that the data interpolation step typically dominates the execution time. In the 3-D imaging example in Section 3.2 (which represents a realistic size for the landing-zone mapping application), performed on a desktop workstation running Windows, the 3-D FFT operation takes less than 1 s, whereas the 3-D interpolation takes several seconds, for a total runtime of about 5 s. One major implementation issue is that the 3-D interpolation cannot be parallelized very efficiently, unlike the 3-D FFT, which is a perfect candidate for vectorization and parallelization. To obtain an efficient parallel implementation on multicore platforms, the interpolation must be broken down into sequences of lower dimensionality.

Optimizing the PFA implementation for execution speed has been outside the scope of this study and we avoid going into further details related to the runtime required by the imaging procedure. Ultimately, the execution time of the imaging formation code depends not only on the hardware architecture and speed, but also on how efficiently some of the key signal processing functions (FFT, interpolation, etc.) are implemented, and whether data vectorization, and implicit or explicit parallelization are used. Future efforts are required to realize the full potential of the PFA for real-time imaging in the challenging 3-D configuration entailed by the FLSAR system.

3.5 Extension to Multistatic Antenna Arrays

An important aspect of the PFA is the assumption that the SAR system operates in a monostatic configuration: that implies we use a pair of collocated Tx and Rx at each sample of the 2-D aperture both in the antenna array and in the forward aperture direction. This represents a useful baseline configuration for the FLSAR system analysis via computer models. However, a practical implementation of the antenna array as a monostatic, uniformly spaced collection of Tx–Rx pairs is very unlikely for obvious reasons related to cost and feasibility.[1] Nevertheless, similar performance with that afforded by a monostatic array can be achieved by multistatic arrays with a lower number of antenna elements.

A typical example of multistatic array for forward-looking radar applications is that employed by the Spectrally Agile Frequency-Incrementing Reconfigurable system,[18] where two Tx elements are placed at the array ends and a number N of Rx elements are uniformly distributed along the array. The Tx elements are activated sequentially in time, whereas all Rx elements receive simultaneously during one pulse transmission. This type of multistatic configuration achieves the same resolution as a monostatic array of the same length (given by Eq. 12b); additionally, the grating lobe spacing is the same as that of a monostatic array made of $2N$ uniformly spaced Tx–Rx pairs.[1] Moreover, as shown by Dogaru et al,[4] the total number of elements can be reduced further by using four Tx and $\frac{N}{2}$ Rx elements, without penalty in the imaging performance metrics.

An analysis of various multistatic antenna array configurations for the FLSAR system is outside the scope of this investigation. Instead, the goal of this section is to establish a general procedure that adapts the PFA to any type of multistatic array geometry. This procedure is based on the theory of multistatic arrays that states the equivalence (as a k-domain data sample) between a bistatic Tx–Rx configuration and a monostatic Tx–Rx configuration, with the equivalent monostatic antenna placed halfway between the bistatic Tx and Rx. (To be rigorous, the equivalent monostatic Tx–Rx pair should be along the bisector of the bistatic Tx–target–Rx angle, but in the MMW radar case the two geometries are practically identical.) Based on this theory, a multistatic array with two Tx elements at the array ends and 64 uniformly spaced Rx elements is equivalent to a monostatic array of 128 uniformly spaced elements and should yield identical images when used in the FLSAR system. Then the radar data obtained by the multistatic array can be recast as the data set obtained by an equivalent monostatic SAR system and subsequently processed by PFA.

Note the length of the propagation path Tx–target–Rx in the bistatic case is slightly different from that of the equivalent monostatic path, as illustrated in Fig. 6. Consequently, the radar signal obtained by the bistatic pair must undergo a phase adjustment to match the phase of the equivalent monostatic pair (note we ignore any magnitude mismatch, which is negligible in practice). The main difficulty with this procedure is that, rigorously speaking, this phase adjustment should depend on the image voxel location; therefore, the phase adjustment cannot be uniformly applied to the radar data as a preprocessing step outside the image formation algorithm. Nevertheless, as we demonstrate in the following paragraphs, the MMW FLSAR system parameters allow us to make certain approximations that render the phase adjustment factor independent of the voxel location. We also present numerical examples to support the accuracy of this procedure.

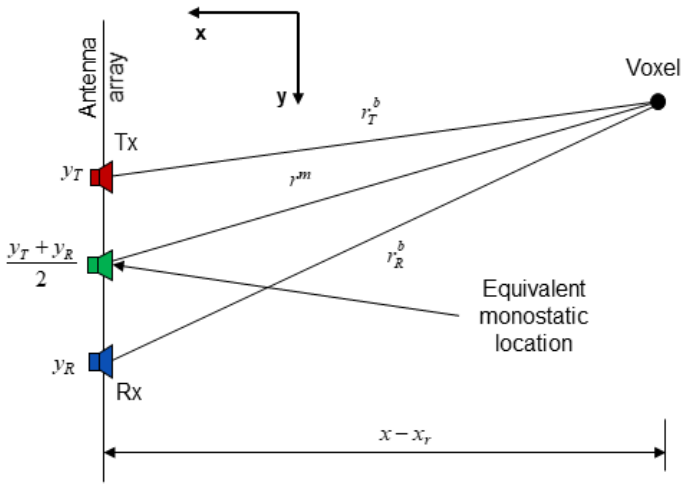

Fig. 6 Geometry involved in the bistatic-to-monostatic transformation via phase adjustment of the radar data

The phase adjustment factor in the bistatic-to-monostatic transformation can be written as $\exp\left(-jk_R\Delta r\right)$, where $\Delta r = 2r^m - r_T^b - r_R^b$ is the difference between the monostatic and bistatic path lengths (see Fig. 6 for reference). In this notation, the superscripts *m* and *b* stand for monostatic and bistatic, respectively, while the subscripts *T* and *R* stand for Tx and Rx, respectively. Let the bistatic Tx and Rx position vectors $\mathbf{r}_T^b = \begin{bmatrix} x_r & y_T & z_r \end{bmatrix}^T$ and $\mathbf{r}_R^b = \begin{bmatrix} x_r & y_R & z_r \end{bmatrix}^T$, while the equivalent monostatic Tx and Rx are both placed at $\mathbf{r}^m = \begin{bmatrix} x_r & \dfrac{y_T+y_R}{2} & z_r \end{bmatrix}^T$. Note only the *y* coordinates of these vectors differ; the subscripts *r* for the *x* and *z* coordinates are generic for "radar". Also let $\left(x, y, z\right)$ the current image voxel coordinates. Given the geometry of the FLSAR system, we can make the following approximations:

$$r_T^b = \sqrt{\left(x-x_r\right)^2 + \left(y-y_T\right)^2 + \left(z-z_r\right)^2} \cong R_A + \frac{\left(y-y_T\right)^2}{2R_A}, \qquad (16a)$$

$$r_R^b = \sqrt{\left(x-x_r\right)^2 + \left(y-y_R\right)^2 + \left(z-z_r\right)^2} \cong R_A + \frac{\left(y-y_R\right)^2}{2R_A}, \qquad (16b)$$

$$\begin{aligned} r^m &= \sqrt{\left(x-x_r\right)^2 + \left(y-\frac{y_T+y_R}{2}\right)^2 + \left(z-z_r\right)^2} \cong R_A + \frac{\left(y-\dfrac{y_T+y_R}{2}\right)^2}{2R_A}, \qquad (16c) \\ &= R_A + \frac{1}{2R_A}\left(y^2 + \frac{y_T^2}{4} + \frac{y_R^2}{4} + \frac{y_T y_R}{2} - yy_T - yy_R\right) \end{aligned}$$

where $R_A = \sqrt{x_r^2 + z_r^2}$. These approximations rely on the fact that the coordinate offset in the y direction $\left|y - y_{T,R}\right|$, as well as the voxel coordinates x and z, are always much smaller than the radar range R_A. By plugging these expressions into the Δr formula and canceling some terms, we obtain

$$\Delta r = 2r^m - r_T^b - r_R^b \cong -\frac{\left(y_T - y_R\right)^2}{4R_A}. \tag{17}$$

Note this approximate expression for the path length difference is independent of the voxel coordinates. The final phase adjustment factor required by the bistatic-to-monostatic transformation is $\exp\left(jk_R \frac{\left(y_T - y_R\right)^2}{4\sqrt{x_r^2 + z_r^2}} \right)$. Since this factor depends on the radar measurement parameters only, it can be applied to the radar data as a preprocessing step outside the main image formation procedure.

The fact that this phase adjustment process is performed outside the image formation algorithm means that it works with any SAR imaging algorithm, not only PFA. For instance, RMA is also based on the monostatic radar assumption (just as PFA), so the bistatic-to-monostatic transformation is required to accommodate multistatic arrays in the system configuration. On the other hand, BPA does not require such transformation since the algorithm can readily handle arbitrary bistatic or multistatic geometries. Nevertheless, we think that BPA can also benefit from applying the bistatic-to-monostatic transformation to the radar data by simplifying some of the radar–voxel range calculations specific to this algorithm.

We successfully tested this procedure on 2-D and 3-D imaging examples involving the FLSAR system. In this section, we only present the 2-D results for the side-looking aperture geometry, which is the one relevant to the multistatic antenna array in the y direction. We use the same system parameters as in Section 3.1, with the exception of the antenna array configuration. This consists of two Tx's at the ends of the 14-m-long array, and 512 Rx's distributed uniformly along the array. The radar data is collected by firing one Tx at a time and receiving on all Rx elements simultaneously. The equivalent monostatic array includes 1024 collocated Tx–Rx pairs, identical to the configuration in Section 3.1.

The result of applying the bistatic-to-monostatic transformation as a preprocessing step to the PFA is shown in Fig. 7. Note the targets are focused at the same coordinates as those in Fig. 3, despite the fact that the phase adjustment factor contains certain approximations. Nevertheless, the reader may raise the issue that the images obtained by PFA contain errors due to the wavefront curvature

phenomenon; therefore, this example cannot be taken as definitive proof that the bistatic-to-monostatic transformation proposed here is accurate enough for our purpose. To address this concern, we applied the WCEC procedure described in Section 4.3. The outcome is shown in Fig. 8: this image demonstrates that all point targets are focused at the correct locations. This result validates the approach to multistatic array imaging developed in this section.

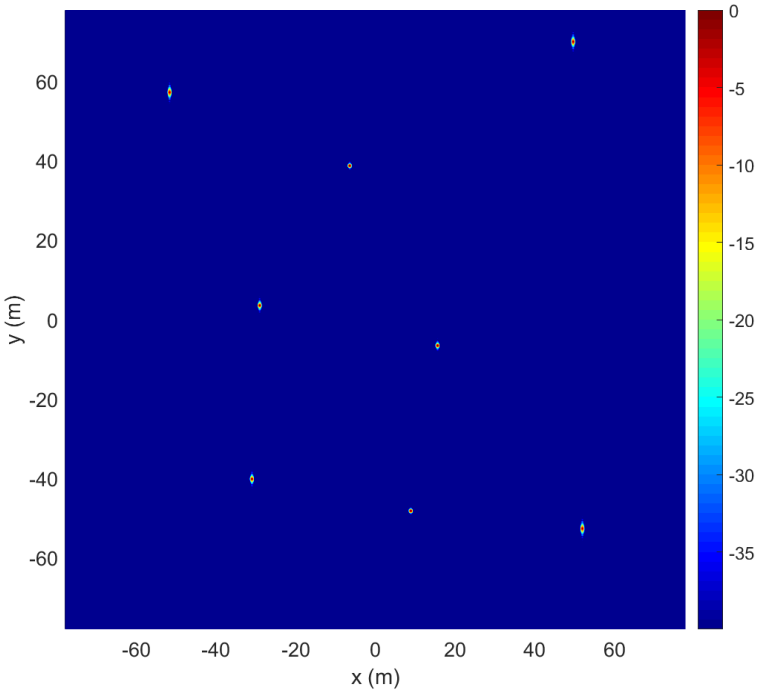

Fig. 7 2-D SAR image obtained by PFA for the side-looking geometry in the x-y plane using a multistatic antenna array and the bistatic-to-monostatic transformation described in this section

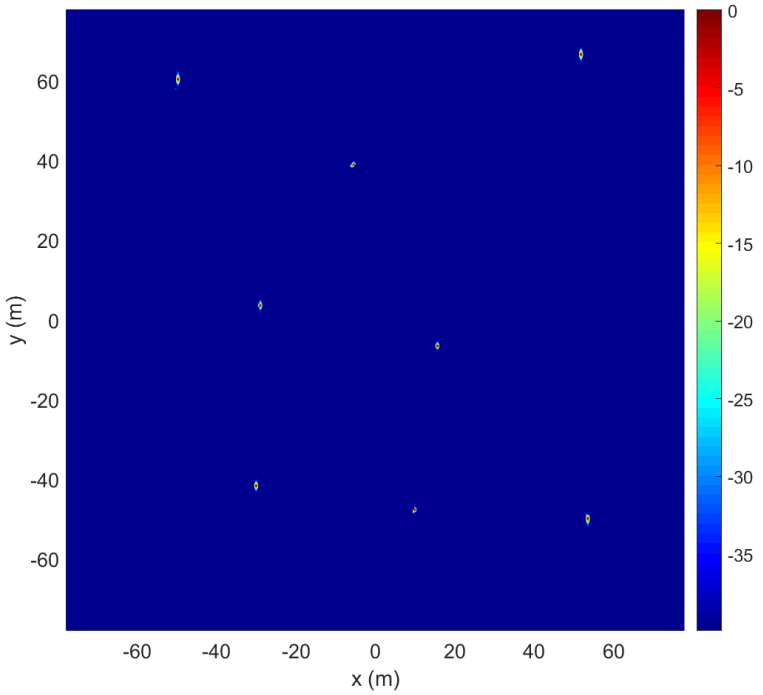

Fig. 8 2-D SAR image obtained by PFA with the WCEC procedure for the side-looking geometry in the x-y plane using a multistatic antenna array and the bistatic-to-monostatic transformation described in this section

4. Wavefront Curvature Error Correction

4.1 Analysis of Wavefront Curvature Phase Errors

Understanding the errors characterizing the SAR system operation and the associated image formation algorithm is essential in designing a robust imaging system that achieves the desired resolution. Since the main part of the radar signal used in SAR imaging is its phase, we are primarily interested in phase errors. There are several ways to categorize the phase errors in SAR systems. For our purpose, we distinguish phase errors induced by platform and target motion as well as phase errors produced by approximations in the radar signal processing algorithms.[5] Examples of the latter include the RVP, specific to compression of LFM waveforms via stretch processing, and the waveform curvature error, which is specific to the PFA and represents the subject of investigation in this section.

Intuitively, the wavefront curvature error arises from the mismatch between the plane wave propagation assumption made by the PFA and the true spherical nature of the radar waves. There are at least two reasons to perform an analytic study of the wavefront curvature errors in PFA: 1) it allows us to derive limits to the image size beyond which the effect of these errors on the image quality becomes

unacceptable, and 2) by quantifying some of these effects, it suggests ways to correct them. For the FLSAR system, we break this analysis into two separate 2-D problems, one dealing with the errors characterizing a side-looking aperture geometry (in the *x*-*y* plane of the FLSAR) and the other dealing with the errors characterizing a forward-looking aperture geometry (in the *x*-*z* plane of the FLSAR). While the wavefront curvature errors in PFA for side-looking apertures constitute a classic topic in SAR analysis that has been investigated by multiple authors,[5–9] extending this analysis to forward-looking apertures is an original contribution of this report.

The algorithmic phase error is typically introduced as a multiplicative factor $\exp\left(-j\psi^e\right)$ that quantifies the difference between the true radar signal phase and the phase assumed by the plane wave approximation specific to the PFA. The phase error term ψ^e can be expressed as a function of the *k*-domain variables. Then the effect of multiplying the radar data by the $\exp\left(-j\psi^e\right)$ factor, which takes place in the *k*-domain, is equivalent to a convolution of the ideal (error-free) radar image with the Fourier transform of this phase error factor[9] (note here we are dealing with 2-D or 3-D convolutions and Fourier transforms, depending on the radar signal dimensionality). By expanding ψ^e in a power series of the *k*-domain variables, we distinguish various types of errors corresponding to the terms in the series (linear, quadratic, cubic, etc.).

Various texts use different ways to express this phase error as a power series. The traditional wavefront curvature error analysis in PFA uses the angular variables (ϕ and θ) to describe the phase error variation along the synthetic aperture.[9] This approach is clearly inadequate for the FLSAR system geometry. A more accurate treatment writes the phase error as a power series of the aperture variables[7] (*u* and *v* in the FLSAR scenario); nevertheless, this methodology is still approximate, since *u* and *v* are not the Fourier counterparts of the image coordinates. The correct approach to analyzing the phase error for a challenging sensing geometry such as that involved by the FLSAR is to express it as a power series of the Cartesian coordinates in the *k*-domain, k_x, k_y, and k_z.[5] The reason why using angular or aperture coordinates does not lead to an accurate phase error analysis is the fact that, for the FLSAR geometry, none of these coordinates is in a linear relationship with the *k*-domain Cartesian coordinates, as already discussed in Section 2.4.

We start by evaluating the difference between the true radar–voxel range, $R = \left|\mathbf{r}_\mathbf{r} - \mathbf{r}\right|$ and the approximation to this range made by the PFA (see Eq. 6), $R^a = r_r - \dfrac{\mathbf{r}_\mathbf{r} \cdot \mathbf{r}}{r_r}$. In these formulas, the position vector

$\mathbf{r_r} = \begin{bmatrix} x_r & y_r & z_r \end{bmatrix}^T = \begin{bmatrix} X_a - u & v & Z_a \end{bmatrix}^T$ describes the radar coordinates and has length r_r, while the position vector $\mathbf{r} = \begin{bmatrix} x & y & z \end{bmatrix}^T$ describes the image voxel coordinates and has length r. For this purpose, we use the following binomial series expansion of R:

$$\begin{aligned} R &= r_r \left| 1 - \frac{\mathbf{r_r} \cdot \mathbf{r}}{r_r^2} \right| = r_r \sqrt{\left(1 - \frac{\mathbf{r_r} \cdot \mathbf{r}}{r_r^2} \right)^2} = r_r \sqrt{1 - 2\frac{\mathbf{r_r} \cdot \mathbf{r}}{r_r^2} + \frac{r^2}{r_r^2}} \\ &= r_r \left[1 - \frac{\mathbf{r_r} \cdot \mathbf{r}}{r_r^2} + \frac{r^2}{2r_r^2} - \frac{\left(\mathbf{r_r} \cdot \mathbf{r} \right)^2}{2r_r^4} + \frac{\left(\mathbf{r_r} \cdot \mathbf{r} \right) r^2}{2r_r^4} - \frac{r^4}{32r_r^4} + \ldots \right]. \\ &= r_r - \frac{\mathbf{r_r} \cdot \mathbf{r}}{r_r} + \frac{r^2}{2r_r} - \frac{\left(\mathbf{r_r} \cdot \mathbf{r} \right)^2}{2r_r^3} + \frac{\left(\mathbf{r_r} \cdot \mathbf{r} \right) r^2}{2r_r^3} - \frac{r^4}{32r_r^3} + \ldots \end{aligned} \tag{18}$$

The range error that characterizes the PFA is then

$$R^e = R - R^a \cong \frac{r^2}{2r_r} - \frac{\left(\mathbf{r_r} \cdot \mathbf{r} \right)^2}{2r_r^3}. \tag{19}$$

The last equation is approximate since we only retained the first two leading terms of the expansion in Eq. 18. These two terms are sufficient in the subsequent phase error analysis of the FLSAR system. The phase error in the $\exp\left(-j\psi^e \right)$ factor previously described in this section is

$$\psi^e = k_R R^e = k_R \left[\frac{r^2}{2r_r} - \frac{\left(\mathbf{r_r} \cdot \mathbf{r} \right)^2}{2r_r^3} \right] = \frac{k_R}{2r_r^3} \left[r^2 r_r^2 - \left(\mathbf{r_r} \cdot \mathbf{r} \right)^2 \right]. \tag{20}$$

At this point, we break the analysis into the 2-D configurations mentioned earlier. First we consider the side-looking geometry in the x-y plane, with fixed u:

$$\begin{aligned} \psi^e &= \frac{k_R}{2r_r^3} \left[\left(x^2 + y^2 \right) \left(X_a^2 + v^2 \right) - \left(x^2 X_a^2 + y^2 v^2 + 2xyX_a v \right) \right] \\ &= k_R \left(\frac{y^2}{2r_r} - \frac{xyX_a}{r_r^3} v + \frac{x^2 - y^2}{2r_r^3} v^2 \right) \end{aligned} . \tag{21}$$

In this equation, we have $r_r = \sqrt{\left(X_a - u \right)^2 + v^2 + Z_a^2}$. At this point, the phase error is expressed in terms of the coordinates k_R and v of the radar measurement. Note Eq. 21 ignores terms in v to a power higher than two.

The next step is to write the phase error in terms of powers of the *k*-domain variables, k_x and k_y. Since the transformation between (k_R, v) and (k_x, k_y) is nonlinear (see Eq. 10), we use a limited Taylor series expansion of $\psi^e(k_x, k_y)$ as follows:

$$\begin{aligned}\psi^e(k_x,k_y) \cong\ & \psi^e(k_{x0},k_{y0}) + \left.\frac{\partial\psi^e}{\partial k_x}\right|_{k_x=k_{x0}} (k_x-k_{x0}) + \left.\frac{\partial\psi^e}{\partial k_y}\right|_{k_y=k_{y0}} (k_y-k_{y0}) \\ & + \frac{1}{2}\left.\frac{\partial^2\psi^e}{\partial k_x^2}\right|_{k_x=k_{x0}} (k_x-k_{x0})^2 + \frac{1}{2}\left.\frac{\partial^2\psi^e}{\partial k_y^2}\right|_{k_y=k_{y0}} (k_y-k_{y0})^2 \\ & + \left.\frac{\partial^2\psi^e}{\partial k_x\partial k_y}\right|_{\substack{k_x=k_{x0}\\k_y=k_{y0}}} (k_x-k_{x0})(k_y-k_{y0})\end{aligned} \quad . \qquad (22)$$

The expansion is performed about the point (k_{x0}, k_{y0}), which represents the radar data support area center in the *k*-domain. This point corresponds to $k_R = k_{R0}$, $u = 0$, and $v = 0$, and has the Cartesian coordinates $k_{x0} = k_{R0}\frac{X_a}{R_a} = k_{R0}\cos\theta_a$ and $k_{y0} = 0$. The variables $k_{xB} = k_x - k_{x0}$ and $k_{yB} = k_y - k_{y0}$ are the "baseband" versions of k_x and k_y and represent the Fourier- (more exactly, the FFT-) coordinate counterparts of the image Cartesian coordinates *x* and *y*, respectively. Before proceeding with the calculations, it is useful to examine the interpretation of the terms in Eq. 22.

The zeroth-order term $\psi^e(k_{x0}, k_{y0})$ is independent of the radar measurement variables (k_x, k_y), so it can be factored outside the 2-D FFT from the *k*-domain to image domain without any impact on the image magnitude.

The first-order terms generate exponential factors of the form $\exp(-ja_x k_{xB})$ and $\exp(-ja_y k_{yB})$. When transformed to the image domain, they become $\delta(x + a_x)$ and $\delta(y + a_y)$, respectively. When these functions are convolved with the error-free image, the effect of the linear phase error terms is to shift the location of the image peak by $(-a_x, -a_y)$, with respect to the true target location.

The second-order terms (also known as the quadratic terms of the phase errors) have the effect of defocusing the target image by widening the main lobe of the PSF. Their effect is similar to the spectrum broadening of a signal that has an LFM (or chirp) component as compared with a purely sinusoidal signal.[9] Note we truncated the Taylor series expansion in Eq. 22 to the second-order terms.

Higher-order terms are typically ignored in the phase error analysis since they are assumed to be small relative to the existing terms.[5] In general, their effect on the SAR image is difficult to separate from the defocusing effect of the quadratic terms.

By applying the chain rule to the partial derivatives, we have

$$\frac{\partial \psi^e}{\partial k_x} = \frac{\partial k_R}{\partial k_x}\frac{\partial \psi^e}{\partial k_R} + \frac{\partial v}{\partial k_x}\frac{\partial \psi^e}{\partial v}, \tag{23a}$$

$$\frac{\partial \psi^e}{\partial k_y} = \frac{\partial k_R}{\partial k_y}\frac{\partial \psi^e}{\partial k_R} + \frac{\partial v}{\partial k_y}\frac{\partial \psi^e}{\partial v}. \tag{23b}$$

The computation of the partial derivatives in Eq. 23, at the point $\left(k_{x0}, k_{y0}\right)$, relies heavily on the PSP. Thus, we have

$$\frac{\partial k_R}{\partial k_x} = \frac{k_x}{k_R} = \frac{X_a - u}{r_r} \quad \text{and} \quad \left.\frac{\partial k_R}{\partial k_x}\right|_{k_x = k_{x0}} = \frac{X_a}{R_a} = \cos\theta_a, \tag{24a}$$

$$\frac{\partial k_R}{\partial k_y} = \frac{k_y}{k_R} = \frac{v}{r_r} \quad \text{and} \quad \left.\frac{\partial k_R}{\partial k_y}\right|_{k_y = k_{y0}} = 0, \tag{24b}$$

$$\frac{\partial v}{\partial k_x} = 0, \tag{24c}$$

$$\frac{\partial v}{\partial k_y} = \frac{r_r}{k_R} \quad \text{and} \quad \left.\frac{\partial v}{\partial k_y}\right|_{k_y = k_{y0}} = \frac{R_a}{k_{R0}}. \tag{24d}$$

$$\frac{\partial \psi^e}{\partial k_R} = \frac{y^2}{2r_r} - \frac{xyX_a}{r_r^3}v + \frac{x^2 - y^2}{2r_r^3}v^2 \quad \text{and} \quad \left.\frac{\partial \psi^e}{\partial k_R}\right|_{\substack{k_R = k_{R0} \\ v=0}} = \frac{y^2}{2R_a}, \tag{24e}$$

$$\frac{\partial \psi^e}{\partial v} = k_R\left(-\frac{xyX_a}{r_r^3} + \frac{x^2 - y^2}{r_r^3}v\right) \quad \text{and} \quad \left.\frac{\partial \psi^e}{\partial v}\right|_{\substack{k_R = k_{R0} \\ v=0}} = -k_{R0}\frac{xyX_a}{R_a^3}. \tag{24f}$$

Finally, the image shifts induced by the linear phase error terms are

$$a_x = \left.\frac{\partial \psi^e}{\partial k_x}\right|_{k_x = k_{x0}} = \frac{y^2 X_a}{2R_a^2} = \frac{y^2}{2R_a}\cos\theta_a, \tag{25a}$$

$$a_y = \left.\frac{\partial \psi^e}{\partial k_y}\right|_{k_y = k_{y0}} = -\frac{xy^2 X_a}{R_a^2} = -\frac{xy}{R_a}\cos\theta_a \,. \tag{25b}$$

Computing the second-order derivatives of the phase error is, so we only show the computation of $\left.\frac{\partial^2 \psi^e}{\partial k_y^2}\right|_{k_y = k_{y0}}$ here. Fortunately, it turns out that $\left.\frac{\partial^2 \psi^e}{\partial k_x^2}\right|_{k_x = k_{x0}} = \left.\frac{\partial^2 \psi^e}{\partial k_x \partial k_y}\right|_{\substack{k_x = k_{x0} \\ k_y = k_{y0}}} = 0$, so only the quadratic error term in k_y has any impact on the image.

$$\begin{aligned} \frac{\partial^2 \psi^e}{\partial k_y^2} &= \left(\frac{\partial k_R}{\partial k_y}\right)^2 \frac{\partial^2 \psi^e}{\partial k_R^2} + 2\frac{\partial k_R}{\partial k_y}\frac{\partial v}{\partial k_y}\frac{\partial^2 \psi^e}{\partial k_R \partial v} + \left(\frac{\partial v}{\partial k_y}\right)^2 \frac{\partial^2 \psi^e}{\partial v^2} \\ &= 2\frac{v}{r_r}\frac{r_r}{k_R}\left(-\frac{xyX_a}{r_r^3} + \frac{x^2 - y^2}{r_r^3}v\right) + \left(\frac{r_r}{k_R}\right)^2 k_R \frac{x^2 - y^2}{r_r^3} \end{aligned} \,. \tag{26}$$

In this equation we used $\frac{\partial^2 \psi^e}{\partial k_R^2} = 0$. We obtain $\left.\frac{\partial^2 \psi^e}{\partial k_y^2}\right|_{\substack{k_R = k_{R0} \\ v=0}} = \frac{x^2 - y^2}{R_a k_{R0}}$. In the case of the quadratic phase error (QPE), we are interested in evaluating the entire corresponding term in Eq. 22:

$$\mathrm{QPE} = \frac{1}{2}\left.\frac{\partial^2 \psi^e}{\partial k_y^2}\right|_{k_y = k_{y0}} \left(k_y - k_{y0}\right)^2 = \frac{1}{2}\frac{x^2 - y^2}{R_a k_{R0}} k_y^2 = \frac{1}{2}\frac{x^2 - y^2}{R_a k_{R0}} k_{R0}^2 \frac{v^2}{R_a^2} = \frac{\left(x^2 - y^2\right) k_{R0} v^2}{2R_a^3} \,. \tag{27}$$

The expressions in Eqs. 25 and 27 match those obtained by Carrara[5] and other authors[6,7] for side-looking SAR geometries. One application of these formulas is in establishing limits on the image domain extent beyond which the phase errors induced by the wavefront curvature phenomenon have a visible impact on the image quality. The first thing to notice about the phase errors described by Eqs. 25 and 27 is that they are space-variant,[5] meaning they depend on the target coordinates (x, y). This fact has important consequences on developing algorithms to compensate for these errors: The phase correction function in these algorithms cannot be applied to the radar data uniformly across the entire image, but must be designed separately for each image pixel/voxel. Further aspects of the WCEC are discussed in Sections 4.2 and 4.3.

In general, Eqs. 25 and 27 indicate that the wavefront curvature phase errors increase with the distance of the target from the Cartesian system origin (or the image center). In the following, we establish the maximum image size for which the impact of these errors on the image is still acceptable. For this purpose, we calculate the maximum "image radius" r_{max}, designated as $r_{\max} = \max\left(x_{\max}, y_{\max}\right)$, where x_{max} and y_{max} are the maximum acceptable pixel coordinates in the x and y directions, respectively (note the image coordinates run from $-x_{max}$ to x_{max} and from $-y_{max}$ to y_{max}).

The criterion for the linear phase error-induced shifts in Eq. 25 is to keep them smaller than the resolution cell size. Thus, we require

$$\left|a_x\right| = \frac{y^2}{2R_a}\cos\theta_a \le \delta x = \frac{c}{2B\cos\theta_a}, \tag{28a}$$

$$\left|a_y\right| = \frac{\left|xy\right|}{R_a}\cos\theta_a \le \delta y = \frac{\lambda_0 R_a}{2L_y}. \tag{28b}$$

In the following, we neglect the factor $\cos\theta_a$, which is very close to 1 for the FLSAR geometry. We obtain the following image size limits based on the linear phase error criterion:

$$r_{\max} = \sqrt{\frac{cR_a}{B}} = \sqrt{2R_a\left(\delta x\right)}, \tag{29a}$$

$$r_{\max} = \sqrt{\frac{\lambda_a R_a^2}{2L_y}} = \sqrt{R_a\left(\delta y\right)}. \tag{29b}$$

Regarding the QPE, we follow other authors in requiring it not to exceed $\frac{\pi}{2}$. This leads to the following condition (obtained when $v = \frac{L_y}{2}$ and either $x = 0$ or $y = 0$):

$$\left|\mathrm{QPE}\right|_{\max} = \frac{r_{\max}^2 k_{R0}}{2R_a^3}\left(\frac{L_y}{2}\right)^2 = \frac{\pi}{2}. \tag{30}$$

From this we derive

$$r_{\max} = \sqrt{\frac{\lambda_0 R_a^3}{L_y^2}} = 2\left(\delta y\right)\sqrt{\frac{R_a}{\lambda_0}}. \tag{31}$$

The final image size limit is twice the smallest of the r_{max} values given by Eq. 29a, 29b, and 31. In the case of the MMW FLSAR proposed by ARL, we have $\delta x \cong \delta y$ and $\delta y >> \lambda_0$; this indicates Eq. 29b sets the most restrictive criterion for the maximum image size in the *x*-*y* plane. We defer further comments on the overall image size limits until after we complete the forward-looking aperture phase error analysis in the *x*-*z* plane.

The wavefront curvature error analysis in the *x*-*z* plane (forward-looking aperture) largely follows the same steps performed for the side-looking aperture. However, one approximation used so far in those derivations, namely neglecting the radar range r_r dependence on the aperture coordinate *v*, cannot be extended to the dependence of r_r in terms of *u* (note *u* may take on significantly larger values than *v* across the radar aperture). This fact makes the phase error calculations for the forward-looking case even more tedious than those for the side-looking case.

A second-order Taylor series expansion similar to that in Eq. 22 holds for the *x*-*z* plane as well:

$$\begin{aligned}\psi^e(k_x,k_z) \cong\ & \psi^e(k_{x0},k_{z0}) + \left.\frac{\partial \psi^e}{\partial k_x}\right|_{k_x=k_{x0}} (k_x-k_{x0}) + \left.\frac{\partial \psi^e}{\partial k_z}\right|_{k_z=k_{z0}} (k_z-k_{z0}) \\ & + \frac{1}{2}\left.\frac{\partial^2 \psi^e}{\partial k_x^2}\right|_{k_x=k_{x0}} (k_x-k_{x0})^2 + \frac{1}{2}\left.\frac{\partial^2 \psi^e}{\partial k_z^2}\right|_{k_z=k_{z0}} (k_z-k_{z0})^2 \\ & + \left.\frac{\partial^2 \psi^e}{\partial k_x \partial k_z}\right|_{\substack{k_x=k_{x0}\\k_z=k_{z0}}} (k_x-k_{x0})(k_z-k_{z0})\end{aligned} \quad . \quad (32)$$

The expansion is performed about the (k_{x0}, k_{z0}) point of coordinates $k_{x0} = k_{R0}\frac{X_a}{R_a} = k_{R0}\cos\theta_a$ and $k_{z0} = k_{z0}\frac{Z_a}{R_a} = k_{R0}\sin\theta_a$. If we fix *v*, the phase error in the *x*-*z* plane derived from Eq. 20 is

$$\begin{aligned}\psi^e &= \frac{k_R}{2r_r^3}\left[\left(x^2+z^2\right)\left(\left(X_a-u\right)^2+Z_a^2\right) - \left(x^2\left(X_a-u\right)^2 + z^2Z_a^2 + 2xz\left(X_a-u\right)Z_a\right)\right] \\ &= k_R\left(\frac{\left(xZ_a - zX_a\right)^2}{2r_r^3} + \frac{xzZ_a - z^2X_a}{r_r^3}u + \frac{z^2-x^2}{2r_r^3}u^2\right)\end{aligned} \quad . \quad (33)$$

Note $r_r = \sqrt{\left(X_a-u\right)^2 + v^2 + Z_a^2}$ is a function of *u*, so the dependence of ψ^e on the aperture coordinate *u* is much more complicated than the quadratic form suggested by Eq. 33. However, to keep the analysis tractable, we rework this formula via a Maclaurin series expansion about the point $u = 0$ to express ψ^e strictly as a quadratic

function of u, as in $\psi^e \cong k_R\left(b_0 + b_1 u + b_2 u^2\right)$. In this expression, similar to that in Eq. 21, we have

$$b_0 = \left.\frac{\psi^e}{k_R}\right|_{u=0} = \frac{\left(xZ_a - zX_a\right)^2}{2R_a^3}, \tag{34a}$$

$$b_1 = \left.\frac{\partial}{\partial u}\left(\frac{\psi^e}{k_R}\right)\right|_{u=0} = \frac{3\left(xZ_a - zX_a\right)^2 X_a + 2\left(xzZ_a - z^2 X_a\right)R_a^2}{2R_a^5}, \tag{34b}$$

$$\begin{aligned} b_2 &= \frac{1}{2}\frac{\partial^2}{\partial u^2}\left(\frac{\psi^e}{k_R}\right)\Bigg|_{u=0} \\ &= \frac{\left(xZ_a - zX_a\right)^2\left(12X_a^2 - 3Z_a^2\right) + 12\left(xzZ_a - z^2 X_a\right)X_a R_a^2 + 2\left(z^2 - x^2\right)R_a^4}{4R_a^7} \end{aligned}. \tag{34c}$$

The explicit calculations of b_0, b_1, and b_2 (not shown here) are tedious but straightforward. Along the way, we used $r_r\big|_{u=0} = R_a$, $\left.\frac{\partial r_r}{\partial u}\right|_{u=0} = -\frac{X_a}{R_a}$, and $\left.\frac{\partial^2 r_r}{\partial u^2}\right|_{u=0} = \frac{Z_a^2}{R_a^3}$. Additional relationships based on the PSP are

$$\frac{\partial k_R}{\partial k_z} = \frac{k_z}{k_R} = \frac{Z_a}{r_r} \quad \text{and} \quad \left.\frac{\partial k_R}{\partial k_z}\right|_{k_z = k_{z0}} = \frac{Z_a}{R_a}; \tag{35a}$$

$$\frac{\partial u}{\partial k_x} = -\frac{Z_a}{k_z} = -\frac{r_r}{k_R} \quad \text{and} \quad \left.\frac{\partial u}{\partial k_x}\right|_{k_x = k_{x0}} = -\frac{R_a}{k_{R0}}; \tag{35b}$$

$$\frac{\partial u}{\partial k_z} = \frac{Z_a k_x}{k_z^2} = \frac{r_r\left(X_a - u\right)}{Z_a k_R} \quad \text{and} \quad \left.\frac{\partial u}{\partial k_x}\right|_{k_x = k_{x0}} = \frac{R_a X_a}{Z_a k_{R0}}. \tag{35c}$$

Now we compute the expansion in Eq. 32 in a manner similar to that in Eq. 22. The image shifts induced by the linear phase error terms are

$$a_x = \left.\frac{\partial \psi^e}{\partial k_x}\right|_{k_x = k_{x0}} = b_0\frac{X_a}{R_a} - b_1 R_a = \frac{\left(zX_a - xZ_a\right)\left(zZ_a + xX_a\right)Z_a}{R_a^4}, \tag{36a}$$

$$a_z = \left.\frac{\partial \psi^e}{\partial k_z}\right|_{k_z = k_{z0}} = b_0\frac{Z_a}{R_a} + b_1\frac{X_a R_a}{Z_a} \cong \frac{\left(zX_a - xZ_a\right)\left(zX_a - 3xZ_a\right)}{2R_a^2 Z_a}. \tag{36b}$$

To calculate the second-order partial derivatives in the QPE terms, we apply the chain rule as in Eq. 26 and obtain

$$\left.\frac{\partial^2\psi^e}{\partial k_x^2}\right|_{k_x=k_{x0}} = \frac{2}{k_{R0}}\left(-X_a b_1 + R_a^2 b_2\right), \tag{37a}$$

$$\left.\frac{\partial^2\psi^e}{\partial k_z^2}\right|_{k_z=k_{z0}} = \frac{2}{k_{R0}}\left(X_a b_1 + \frac{X_a^2 R_a^2}{Z_a^2} b_2\right), \tag{37b}$$

$$\left.\frac{\partial^2\psi^e}{\partial k_x \partial k_z}\right|_{\substack{k_x=k_{x0}\\k_z=k_{z0}}} = \frac{2}{k_{R0}}\left(\frac{X_a^2 - Z_a^2}{2Z_a} b_1 - \frac{X_a R_a^2}{Z_a} b_2\right). \tag{37c}$$

Upon a closer examination, the terms containing b_2 in the Eq. 37 formulas are dominant; therefore, we neglect the terms containing b_1. The full QPE terms in the phase error expansion can be approximated as follows:

$$\mathrm{QPE}_{x^2} = \frac{1}{2}\left.\frac{\partial^2\psi^e}{\partial k_x^2}\right|_{k_x=k_{x0}} \left(k_x - k_{x0}\right)^2 \cong k_{R0} b_2 u^2, \tag{38a}$$

$$\mathrm{QPE}_{z^2} = \frac{1}{2}\left.\frac{\partial^2\psi^e}{\partial k_z^2}\right|_{k_z=k_{z0}} \left(k_z - k_{z0}\right)^2 \cong k_{R0}\frac{X_a^4}{R_a^4} b_2 u^2, \tag{38b}$$

$$\mathrm{QPE}_{xz} = \left.\frac{\partial^2\psi^e}{\partial k_x \partial k_z}\right|_{\substack{k_x=k_{x0}\\k_z=k_{z0}}} \left(k_x - k_{x0}\right)\left(k_z - k_{z0}\right) \cong 2k_{R0}\frac{X_a^2}{R_a^2} b_2 u^2. \tag{38c}$$

In establishing these formulas, we used the approximations $k_x - k_{x0} \cong -k_{R0}\dfrac{u}{R_a}$ and $k_z - k_{z0} \cong k_{R0}\dfrac{Z_a X_a u}{R_a^3}$. Since we have $\dfrac{X_a}{R_a} \cong 1$, the expressions in Eqs. 38a and 38b are approximately equal, and half of the expression in Eq. 38c. One could notice that we made a significant number of approximations throughout the QPE derivation for the forward-looking aperture, which may call into question the accuracy of these calculations. Nevertheless, this procedure is adequate for our final purpose in this section, which is to estimate limits of the image extent for which the impact of the phase errors is still acceptable. To establish these limits, we use similar criteria as in the side-looking aperture analysis.

Since now the expressions of the image coordinate shifts a_x and a_z, as well as those of the QPE have a more complex dependence on the target coordinates x and z, we

need to be more diligent in finding the maximum acceptable image dimensions than in the side-looking case. In general, we expect the maximum phase errors to occur along the image edges or at the image corners. To simplify the calculations, we consider the following three cases: 1) take $x = 0$ and find z_{max}, 2) take $z = 0$ and find x_{max}, and 3) take $x = \pm z$ and find x_{max} and z_{max}. Then, by comparing the three criteria (on the maximum acceptable values for a_x, a_z and QPE, respectively), we pick the most restrictive ones on both x_{max} and z_{max}.

First consider $|a_x| \le \delta x$ when $x = 0$. We obtain $|a_x| \cong \frac{z^2 Z_a^2}{R_a^3}$ and $z_{\max} = \sqrt{\frac{R_a^3 (\delta x)}{Z_a^2}}$. The same criterion with $z = 0$ yields $|a_x| \cong \frac{x^2 Z_a^2}{R_a^3}$ and $x_{\max} = \sqrt{\frac{R_a^3 (\delta x)}{Z_a^2}}$. When $x = \pm z$, $|a_x| \cong \frac{xz Z_a}{R_a^2}$ and $x_{\max} = z_{\max} = \sqrt{\frac{R_a^2 (\delta x)}{Z_a}}$. Note the latter limits for x_{max} and z_{max} are smaller (more restrictive) than the former, so we keep them as the image extent limits derived from $|a_x| \le \delta x$.

Next, we consider $|a_z| \le \delta z$ when $x = 0$. This implies $|a_z| \cong \frac{z^2}{2Z_a}$ and $z_{\max} = \sqrt{2Z_a (\delta z)}$. For $z = 0$, the same criterion yields $|a_z| \cong \frac{3x^2 Z_a}{2R_a^2}$ and $x_{\max} = \sqrt{\frac{2R_a^2 (\delta z)}{3Z_a}}$. For $x = \pm z$, $|a_z| \cong \frac{z^2}{2Z_a}$ and $x_{\max} = z_{\max} = \sqrt{2Z_a (\delta z)}$.

So far, comparing the image extent limits obtained from the linear phase error terms, and taking into account that $\delta x \cong \delta z$ and $R_a >> Z_a$, we notice that the smallest values for x_{max} and z_{max} are given by $\sqrt{2Z_a (\delta z)}$. If in turn we compare this formula with those in Eq. 29 (i.e., $x_{\max} = \sqrt{2R_a (\delta x)}$ and $y_{\max} = \sqrt{R_a (\delta y)}$), we infer that when it comes to keeping the wavefront curvature errors within acceptable bounds, the forward-looking configuration introduces more-restrictive limits to the image size than the side-looking configuration. For the full 3-D geometry of the FLSAR, the linear phase error terms set the following limits on the image size:

$$D_x^{\max} = 2x_{\max} = 2\sqrt{2Z_a (\delta z)}, \tag{39a}$$

$$D_y^{\max} = 2y_{\max} = 2\sqrt{R_a (\delta y)}, \tag{39b}$$

$$D_z^{\max} = 2z_{\max} = 2\sqrt{2Z_a(\delta z)}. \tag{39c}$$

The QPE in the forward-looking case is approximately the same in the x and z directions, so it suffices to analyze one of them by requiring $|\text{QPE}| \le \frac{\pi}{2}$. For $x = 0$, we obtain $|\text{QPE}| \cong \frac{k_{R0} z^2 u^2}{2R_a^3}$ and $z_{\max} = \sqrt{\frac{\lambda_0 R_a^3}{L_x^2}} = 2(\delta z)\sqrt{\frac{Z_a^2}{\lambda_0 R_a}}$. For $z = 0$, we obtain $|\text{QPE}| \cong \frac{k_{R0} x^2 u^2}{2R_a^3}$ and $x_{\max} = \sqrt{\frac{\lambda_0 R_a^3}{L_x^2}} = 2(\delta z)\sqrt{\frac{Z_a^2}{\lambda_0 R_a}}$. For $x = \pm z$, we obtain $|\text{QPE}| \cong \frac{6k_{R0} x^2 u^2 (R_a - X_a)}{2R_a^4}$ and $x_{\max} = z_{\max} = \sqrt{\frac{\lambda_0 R_a^4}{6L_x^2 (R_a - X_a)}}$. For typical FLSAR parameters, the most-restrictive limits obtained from the QPE criterion are $x_{\max} = z_{\max} = 2(\delta z)\sqrt{\frac{Z_a^2}{\lambda_0 R_a}}$. These limits are smaller than the ones set by the QPE criterion in Eq. 31 for the side-looking geometry but larger than those obtained from the linear phase error terms in Eq. 39.

As a numerical example, we take the following typical FLSAR parameters: $\delta y = \delta z = 0.3$ m, $R_a = 150$ m, $Z_a = 26$ m, and $f_0 = 35$ GHz. Then, the linear phase error terms yield (Eq. 39) $D_x^{\max} = D_z^{\max} = 7.9$ m and $D_y^{\max} = 13.4$ m, while the QPE terms yield $D_x^{\max} = D_z^{\max} = 25.4$ m and $D_y^{\max} = 147$ m. It is clear that keeping the linear phase errors under acceptable limits sets more-restrictive conditions for the image size than the QPE criterion. Moreover, if the desired radar image extent is no larger than 25 m in each dimension, a phase error correction algorithm can largely ignore the QPE and simply focus on compensating the linear phase error terms.

Note other authors[5] mostly ignore the restrictions on image size introduced by the linear phase errors based on the fact that (at least theoretically) these errors can be corrected by a relatively straightforward procedure. Consequently, they only consider the QPE produced by the wavefront curvature when setting the size limits of a SAR image created with the PFA. Nevertheless, as we show in the following sections, implementing an accurate correction procedure for the linear phase errors of a high-resolution FLSAR system is far from trivial and in fact requires strict observance of the limits set by Eq. 39.

Note also the image size limits obtained by keeping the wavefront curvature errors of PFA under certain bounds are very different from the limits set by the traditional far field criterion, $D = \sqrt{\frac{R_a \lambda_0}{2}}$. When evaluated for typical FLSAR parameters, this

formula yields a maximum image size of 0.8 m, which is clearly much smaller than all the figures obtained by wavefront curvature error analysis. Therefore, the traditional far-field condition provides a flawed criterion in deciding the applicability of the PFA to an SAR imaging configuration; instead, the methodology presented in this section proposes a much more accurate approach to making this decision.

To conclude this section, we verify the accuracy of the image coordinate shifts predicted by Eqs. 25 and 36. The reason for this check will become apparent in Section 4.4, where we discuss a possible WCEC procedure based on these computations. We perform this verification separately for the side-looking and forward-looking geometries, using the 2-D numerical imaging examples from Section 3.1. Table 3 lists the target coordinate shifts obtained in the SAR images created by the uncorrected PFA in Section 3.1 as well as the numerical values estimated by Eqs. 25 and 36 (the image coordinate shifts are actually the negative of a_x, a_y, and a_z, respectively). Note the target coordinates in the SAR images in Figs. 3 and 4 can only be determined with a precision of about half a resolution cell (0.15 m). Consequently, we expect a match between the shifts in Table 3 of this order of magnitude. For the same reason, we round off all the coordinate values to one decimal point. For most of the point targets considered in these examples, the match between the image shifts and the predictions based on Eqs. 25 and 36 is very good (within 0.2 m). However, there are two targets for which the predictions differ from the PFA images by a larger margin: Target 6 in the side-looking case and Target 1 in the forward-looking case. We attribute these discrepancies to the truncation of the power series expansion of the radar–voxel range in Eq. 18. For large absolute values of the target coordinates (x, y, z), higher-order terms in that expansion become significant and may need to be included in the subsequent calculations. However, this approach is not pursued any further in this study.

Table 3 Target image shifts induced by the wavefront curvature phase error in the PFA, for the 2-D side-looking and forward-looking SAR configurations, listing the true shifts in the images in Figs. 3 and 4 and their values estimated by Eqs. 25 and 36

Target number	Side-looking				Forward-looking			
	True shifts		Estimated shifts		True shifts		Estimated shifts	
	x (m)	y (m)	x (m)	y (m)	x (m)	z (m)	x (m)	z (m)
1	–1.8	–2.9	–1.8	–2.9	0.4	–7.3	0.4	–6.6
2	–2.4	3.4	–2.2	3.4	–0.1	0.4	–0.2	0.4
3	–0.1	–0.1	0	–0.1	0.1	–1.7	0	–1.6
4	–1.1	–0.4	–1.1	–0.5	0	–6.3	0	–6.4
5	0	–0.1	0	–0.1	0	–0.4	0	–0.4
6	–0.9	0.8	–0.8	1.2	–0.2	–2.1	–0.2	–2.3
7	–1.3	–2.7	–1.2	–2.6	–0.1	–4.4	0	–4.4
8	–0.9	–0.2	–0.7	–0.2	0	0	0	0

4.2 Wavefront Curvature Error Correction Procedure

In this report, we develop the WCEC as a postprocessing technique that starts with the uncorrected image created by PFA, as described in Section 2.4. This procedure is equivalent with a multiplication of the radar data by the factor $\exp\left(j\psi^e\right)$, which compensates for the wavefront curvature phase error analyzed in Section 4.1. Other possible approaches to WCEC are presented in Section 4.4.

In the previous section, we expressed the phase error ψ^e as a function of the *k*-domain variables $\left(k_x, k_y, k_z\right)$. That means we can start with the *k*-domain image data, obtained after the interpolation step in PFA, and apply the factor $\exp\left(j\psi^e\right)$ to compensate for the phase error before the Fourier transform to the image domain. This *k*-domain multiplication represents an image filtering operation, where $\exp\left(j\psi^e\right)$ is the filter's transfer function. The main issue with this procedure is the fact that ψ^e depends on the voxel coordinates $\left(x, y, z\right)$—this is the space-variant aspect of the wavefront curvature phase error mentioned earlier—therefore applying the $\exp\left(j\psi^e\right)$ factor computed for a specific voxel only corrects the error at that voxel location. Moving to a different voxel involves recalculating ψ^e and reapplying the correction filter to the entire *k*-domain image.

Obviously, this way of approaching the WCEC is extremely inefficient and cannot be turned into a practical implementation procedure. To obtain a reasonably fast WCEC algorithm, we break the entire image into subimages of limited size, and apply a single correction filter to an entire subimage at one time. The key to this implementation is to make sure that each subimage size does not exceed the limits established in Section 4.1 for which the phase errors are still acceptable. The details

of the subimage-oriented WCEC procedure are discussed in the following section. In the current section, we establish the correction filter's transfer function for a specific voxel at coordinates (x, y, z).

A somewhat similar WCEC procedure is described by Doerry,[7] who uses the power series expansion of the phase error ψ^e in the correction filter's transfer function. Note Doerry expresses ψ^e in terms of the aperture coordinates, which is not as rigorous as using powers of the *k*-domain Cartesian variables and does not lead to an accurate analysis in the case of the FLSAR geometry, as discussed in Section 4.1. Moreover, even if we used the formulas established in that section as power series of the *k*-domain variables, those formulas are still approximate and ignore higher-order power terms in those variables, which may have a significant contribution to the phase error in certain scenarios. To avoid these issues, we develop a novel, rigorous *k*-domain WCEC filter based on an idea by Soumekh,[10] adapted to the FLSAR configuration.

The WCEC filter's transfer function can be written as

$$H\left(k_x, k_y, k_z\right) = \exp\left(j\psi^e\right) = \exp(jk_R R^e) = \exp\left(j\sqrt{k_x^2 + k_y^2 + k_z^2}\, R^e\right). \quad (40)$$

To determine the range error R^e we avoid making any of the approximations in Section 4.1 by using the exact formula

$$\begin{aligned} R^e = R - R^a = &\sqrt{\left(x_r - x_0\right)^2 + \left(y_r - y_0\right)^2 + \left(z_r - z_0\right)^2} \\ &-\sqrt{x_r^2 + y_r^2 + z_r^2} + \frac{x_0 x_r + y_0 y_r + z_0 z_r}{\sqrt{x_r^2 + y_r^2 + z_r^2}} \end{aligned}, \quad (41)$$

where (x_0, y_0, z_0) are the coordinates of the voxel for which the filter is designed. At this stage in our derivation, the range error depends on the radar coordinates (x_r, y_r, z_r); however, we would like to express this error as a function of (k_x, k_y, k_z) instead. Fortunately, the two sets of coordinates are related to one another by a set of equations that allow us to uniquely determine (x_r, y_r, z_r) from (k_x, k_y, k_z). First, based on PSP, we can write

$$\frac{x_r}{k_x} = \frac{y_r}{k_y} = \frac{z_r}{k_z}. \quad (42)$$

The third equation constrains the radar antenna position to move across a surface of equation $f(x_r, y_r, z_r) = 0$, which we call the aperture surface. These three equations allow us to find the coordinates (x_r, y_r, z_r) for a given sample in the (k_x, k_y, k_z) space, and replace those in Eq. 41. Note a closed-form solution to these equations may not exist for an arbitrary shape of the aperture surface (or function $f(x_r, y_r, z_r)$). However, in the FLSAR case, this surface is simply described by the equation $z_r = Z_a$, where Z_a is the constant aperture height. Now we can find x_r and y_r as follows:

$$x_r = Z_a \frac{k_x}{k_z} \ , \ y_r = Z_a \frac{k_y}{k_z}. \tag{43}$$

The full expression of the range error as a function of (k_x, k_y, k_z) becomes

$$\begin{aligned} R^e = & \sqrt{\left(Z_a \frac{k_x}{k_z} - x_0 \right)^2 + \left(Z_a \frac{k_y}{k_z} - y_0 \right)^2 + \left(Z_a - z_0 \right)^2} \\ & - \frac{Z_a}{k_z} \sqrt{k_x^2 + k_y^2 + k_z^2} + \frac{x_0 k_x + y_0 k_y + z_0 k_z}{\sqrt{k_x^2 + k_y^2 + k_z^2}} \end{aligned} . \tag{44}$$

This formula can be plugged into Eq. 40 to obtain an expression for the WCEC filter's transfer function that now contains only the *k*-domain coordinates and fixed spatial coordinates: (x_0, y_0, z_0) and Z_a.

For completeness, we now list the range error expressions as a function of *k*-domain variables for the 2-D imaging cases considered in Section 3.1: the side-looking aperture geometry in the *x*-*y* plane and the forward-looking aperture geometry in the *x*-*z* plane. Thus, for the 2-D side-looking aperture case, we have

$$\begin{aligned} R^e = & \sqrt{\left(X_a - x_0 \right)^2 + \left(X_a \frac{k_y}{k_x} - y_0 \right)^2 + \left(Z_a - z_0 \right)^2} \\ & - \sqrt{X_a^2 \left(1 + \frac{k_y^2}{k_x^2} \right) + Z_a^2} + \frac{X_a \left(x_0 + y_0 \frac{k_y}{k_x} \right) + z_0 Z_a}{\sqrt{X_a^2 \left(1 + \frac{k_y^2}{k_x^2} \right) + Z_a^2}} \end{aligned} . \tag{45}$$

For the 2-D forward-looking aperture in the *x*-*z* plane, we have

$$R^e = \sqrt{\left(Z_a \frac{k_x}{k_z} - x_0\right)^2 + \left(Z_a - z_0\right)^2} - \frac{Z_a}{k_z}\sqrt{k_x^2 + k_z^2} + \frac{x_0 k_x + z_0 k_z}{\sqrt{k_x^2 + k_z^2}}. \quad (46)$$

We implemented these *k*-domain WCEC filters for all the imaging examples presented in Sections 3.1 and 3.2, involving 2-D images in side-looking and forward-looking aperture configurations, respectively, and 3-D images obtained by the FLSAR system. In all cases, the *k*-domain WCEC was implemented for one target location at a time. All numerical simulations demonstrated perfect match between the true target coordinates and its location in the image after the correction. Nevertheless, as previously discussed, this procedure of designing a separate filter for each image voxel is not a practical implementation solution. A more feasible approach to the WCEC implementation is presented in the next section.

4.3 Implementation of the Subimage-Oriented WCEC Procedure

The principle of the subimage-oriented WCEC procedure was briefly described in the previous section. Thus, the entire uncorrected image is broken into subimages of smaller size, and a correction filter is applied to all voxels within a subimage with separate filters designed for each subimage. In the end, the subimages are reassembled together to form the final, corrected image. Each correction filter is designed to exactly compensate the phase error for the voxel located at the corresponding subimage center. Additionally, the subimage size is chosen such that the phase errors characterizing voxels at its edges do not exceed the limits established in Section 4.1.

Two types of implementation are possible for the phase correction filters: in the *k*-domain (which corresponds to the frequency domain in filter theory) or in the image domain (which corresponds to the time domain in filter theory). After investigating both types of implementations, we concluded that the *k*-domain version is computationally inefficient despite the benefits of using multidimensional FFTs to switch back and forth between the image- and *k*-domains. The reason is that, when transformed from the image to the *k*-domain, the image data characterizing a limited-size subimage still occupies the entire radar data *k*-domain support area/volume. Consequently, the operations involved by this procedure (multidimensional FFTs and multiplication by the correction filter's transfer function) must be performed on the entire *k*-domain image size for each separate subimage. If we have to deal with a large number of subimages, this procedure becomes computationally cumbersome and therefore is not a good practical method to implement the WCEC.

A more efficient WCEC procedure can be obtained in the image domain by employing FIR filters.[15] The impulse response of these filters is obtained as the inverse Fourier transform of the transfer function given by one of Eqs. 44–46. The filtering operation now consists of a multidimensional (2-D or 3-D) convolution[19] of the subimage data with the filter's impulse response. As long as the latter can be represented by a small number of coefficients, this WCEC scheme involves reduced computational complexity because the processing is applied to data blocks of the subimage size at one time.

For the full 3-D FLSAR geometry, the FIR filter design starts with the transfer function in Eq. 44, where (x_0, y_0, z_0) are the coordinates of the voxel in the current subimage center. We apply the windowing FIR design method,[15] which consists of taking an inverse 3-D FFT of the transfer function and applying a finite-length, tapered window to the image domain impulse response. Numerical experiments have shown that a filter length of 12 coefficients in each Cartesian direction is sufficient to obtain satisfactory results by this WCEC procedure. Graphic representations of a typical FIR filter nontruncated impulse response are shown in Fig. 9. These diagrams show the variation of the filter's coefficients corresponding to Target 1 in the 2-D side-looking (*x*-*y* plane) and forward-looking (*x*-*z* plane) configurations, respectively (see Tables 1 and 2 for a list of the target coordinates).

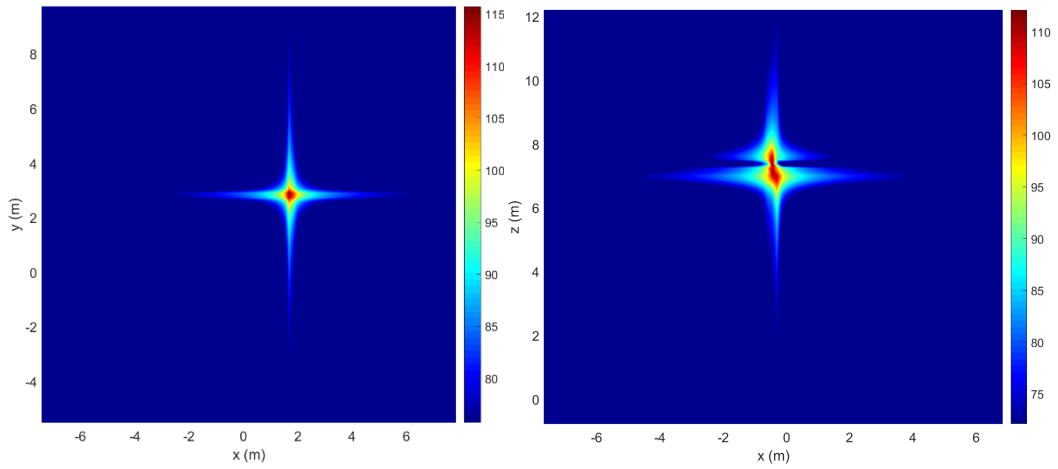

Fig. 9 Representation of the WCEC FIR filter impulse response magnitude for the 2-D imaging examples in Section 3.1: a) side-looking configuration (x-y plane), and b) forward-looking configuration (x-z plane). Both filters are designed for Target 1 in each of those numerical examples.

Note if the phase error ψ^e only contained linear terms in the *k*-domain variables, the correction FIR filter's impulse response would consist of a 3-D delta function centered at the (a_x, a_y, a_z) coordinates, which represent the negative of the voxel

shifts induced by the wavefront curvature phase error. In that case, the filtering operation in the image domain would simply perform a shift of each voxel by these distances to the corrected location. This seems to be largely the case for the *x*-*y* plane filter obtained in the side-looking configuration, shown in Fig. 9a. Nevertheless, quadratic and higher-order terms are also present in ψ^e and must be compensated for by the WCEC procedure. Consequently, the true impulse response may depart from a delta function as demonstrated by the forward-looking example in Fig. 9b. In that case, the filter performs an image refocusing task besides the voxel coordinate shift (note the impulse response phase, which was not represented in Fig. 9, plays an important role in this procedure). Since the quadratic and higher-order terms have small magnitudes relative to the linear terms, the FIR filter coefficients decrease very fast away from the center location, which justifies the truncation of the impulse response to a small number of coefficients.

The filter design procedure does not depend on the radar data or image, so it can be performed offline (outside the main radar image processing data stream) and the filter coefficients stored for subsequent usage in the convolutions with the subimage data. To make sure we do not miss any important region of the *k*-domain image data support, the inverse FFT of the transfer function is performed over the entire *k*-domain support volume for each subimage filter. Although this filter design procedure is somewhat slow, the fact that it is executed offline means it does not have any impact on the overall efficiency of the WCEC algorithm.

The multidimensional convolutions of the subimage data with the filter impulse response are implemented in MATLAB[16] using the function *convn*, which performs the N-dimensional convolution of two N-dimensional data arrays (in our cases, N equals 2 or 3). One should note that the MATLAB convolution implementation is very efficient and capable of simultaneously using multiple computational cores via data vectorization. The author's own attempts to implement multidimensional convolutions from scratch resulted in relatively inefficient code, which is difficult to parallelize due to the inseparability of coordinates characterizing the multidimensional convolution operations.[19]

A number of details related to choosing the subimage extent and position must be observed in the WCEC procedure to ensure the algorithm's accuracy and efficiency:

- The FIR filter impulse response coefficients for one specific subimage are not centered in the Cartesian coordinate origin but at coordinates $\left(a_x, a_y, a_z\right)$. One way to simplify the filter coefficient storage and subsequent convolutions is to simultaneously shift the filter's impulse

response and the original subimage coordinates by $\left(-a_x, -a_y, -a_z\right)$, such that the impulse response is now centered in the origin. The subimage coordinate shifting is illustrated in Fig. 10, which schematically shows the location of the current subimage within the entire image before and after the WCEC procedure. Note that the subimage partition process starts with the output image; the location of each input subimage is computed by shifting the corresponding output subimage coordinates by appropriate quantities.

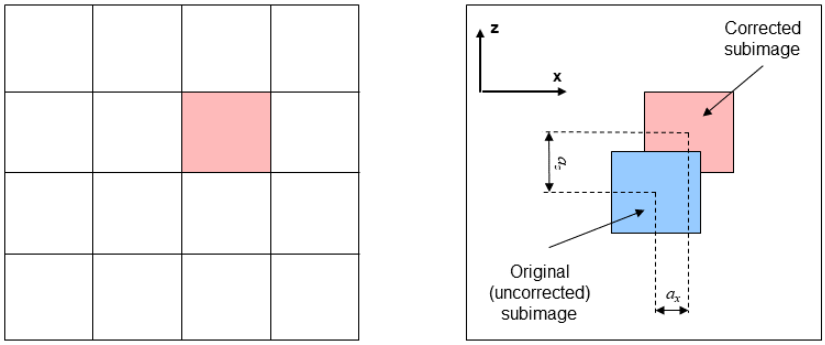

Fig. 10 Illustration of the subimage coordinate shifting within the WCEC procedure, showing the subimage position in the corrected image (left) and the corresponding subimage in the original (uncorrected) image (right)

- Because of this subimage coordinate shifting, the original (uncorrected) SAR image (regarded as a multidimensional data array) must be extended by appropriate margins in all dimensions to accommodate the coordinate shifts. These shifts can be approximately predicted by Eqs. 25 and 36. However, a more accurate method of finding the coordinate shifts is to record the locations of the impulse response peaks obtained in the filter design procedure described in this section. Our numerical experiments showed that the additional image margins required by the 2-D forward-looking configuration can sometimes reach a large number of voxels (close to 100), particularly in the *z* direction.

- The convolution of the subimage data array with a filter impulse response of length (or filter order) M extends the array by M –1 voxels in each dimension. This fact needs to be accounted for in sizing the original subimage patches, while the corrected subimages at the output of the convolution operation need to be trimmed back to the nominal patch size.

- Ideally, the uncorrected, shifted subimages used as an input to the WCEC algorithm should form a perfect set of tiles covering the original SAR image, meaning there should be no overlaps or gaps between those subimages. If there are overlaps between two subimages, a target placed

within the overlap region in the uncorrected image would be processed twice by two different FIR filters introducing slightly different coordinate shifts. That would result in the target appearing twice at different locations in the final, composite SAR image. Gaps in coverage could mean that targets placed in those gaps in the uncorrected image would be missed in the final image. Ensuring perfect subimage tiling consists of a very tedious coding task, but is essential in avoiding the introduction of image artifacts by the WCEC procedure.

The most serious difficulty we encountered in implementing the subimage-oriented WCEC algorithm described in this section occurs when a target straddles the boundary between two subimages. If the voxel size were chosen equal to the resolution cell size, a point target image would always be strictly contained in one subimage (assuming perfect subimage tiling as previously discussed). In that case, there would be a one-to-one correspondence between the target images in the uncorrected and corrected SAR images. However, as indicated in Section 3.3, this method of choosing the voxel size is not recommended; instead, the voxel size should be made a fraction of the resolution cell size, meaning that a point target image would extend over several voxels. When these voxels cross the boundary between two subimages, the target splits into two separate parts in the final, corrected image.

At the current stage of this investigation we have not been able to find a satisfactory solution to the split target image issue within the subimage-oriented processing framework. This phenomenon introduces artifacts in the corrected SAR image manifested as discontinuities around the subimage boundaries. One possible way to decrease the phase errors (and the resulting coordinate shifts) for voxels at the edges of each subimage is to reduce the subimage size. This would result in smaller coordinate shifts for voxels at the subimage edges which in turn would bring the two parts of the target closer together in the final image. Nevertheless, decreasing the subimage size produces an increased number of subimages and boundaries between these subimages. The consequence is a rise in discontinuity regions in the final image, which end up degrading the image quality instead of improving it. Several alternative approaches to the WCEC problem are presented in Section 4.4.

We conclude this section with numerical examples illustrating the WCEC procedure as applied to the images created by PFA in Sections 3.1 and 3.2. Figure 11 shows the corrected version of the image in Fig. 3 obtained for a 2-D side-looking aperture configuration in the x-y plane. In this case, we break the original image into 16×16 subimages in the x and y directions, respectively, with each subimage of size 9.75×9.75 m. Figure 12 shows the corrected counterpart of the image in Fig. 4 representing a 2-D forward-looking aperture configuration in

the *x*-*z* plane. In this case, we break the original image into 16 × 24 subimages in the *x* and *z* directions, respectively, with each subimage of size 9.75 × 5.33 m. Table 4 lists the target image coordinates after applying the WCEC procedure for the 2-D configurations. In general, the target locations in the new images match their true coordinates very well with better than 0.2 m accuracy. However, two targets still exhibit coordinate shifts of 0.3 m (which is comparable to one resolution cell): Target 1 in the side-looking case and Target 4 in the forward-looking case.

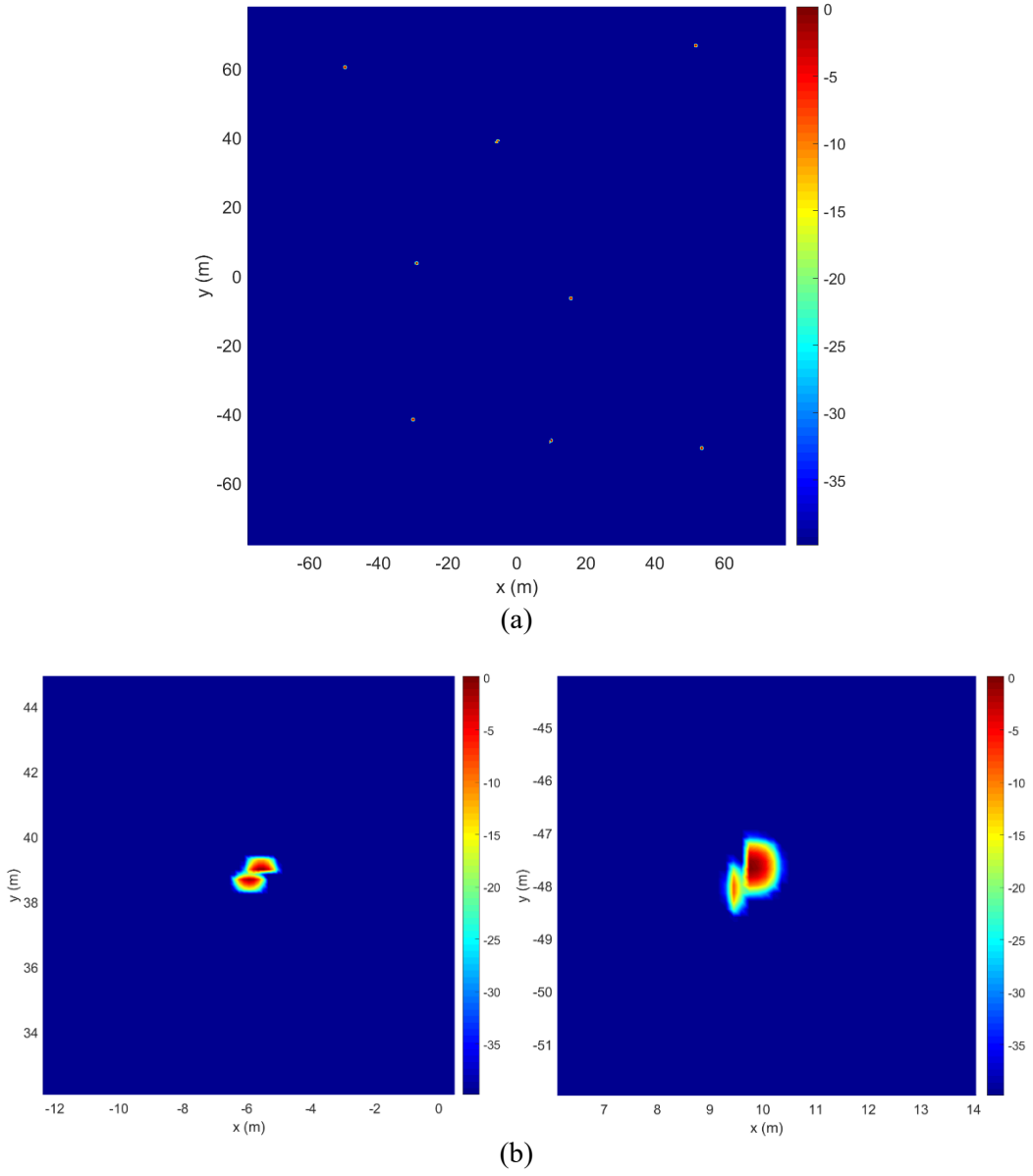

Fig. 11 2-D SAR image obtained by PFA and the WCEC procedure for the side-looking geometry in the x-y plane, for the same point target set as in Fig. 3, showing a) the full image and b) details around two targets exhibiting the split image issue. None of the other target images displays this issue.

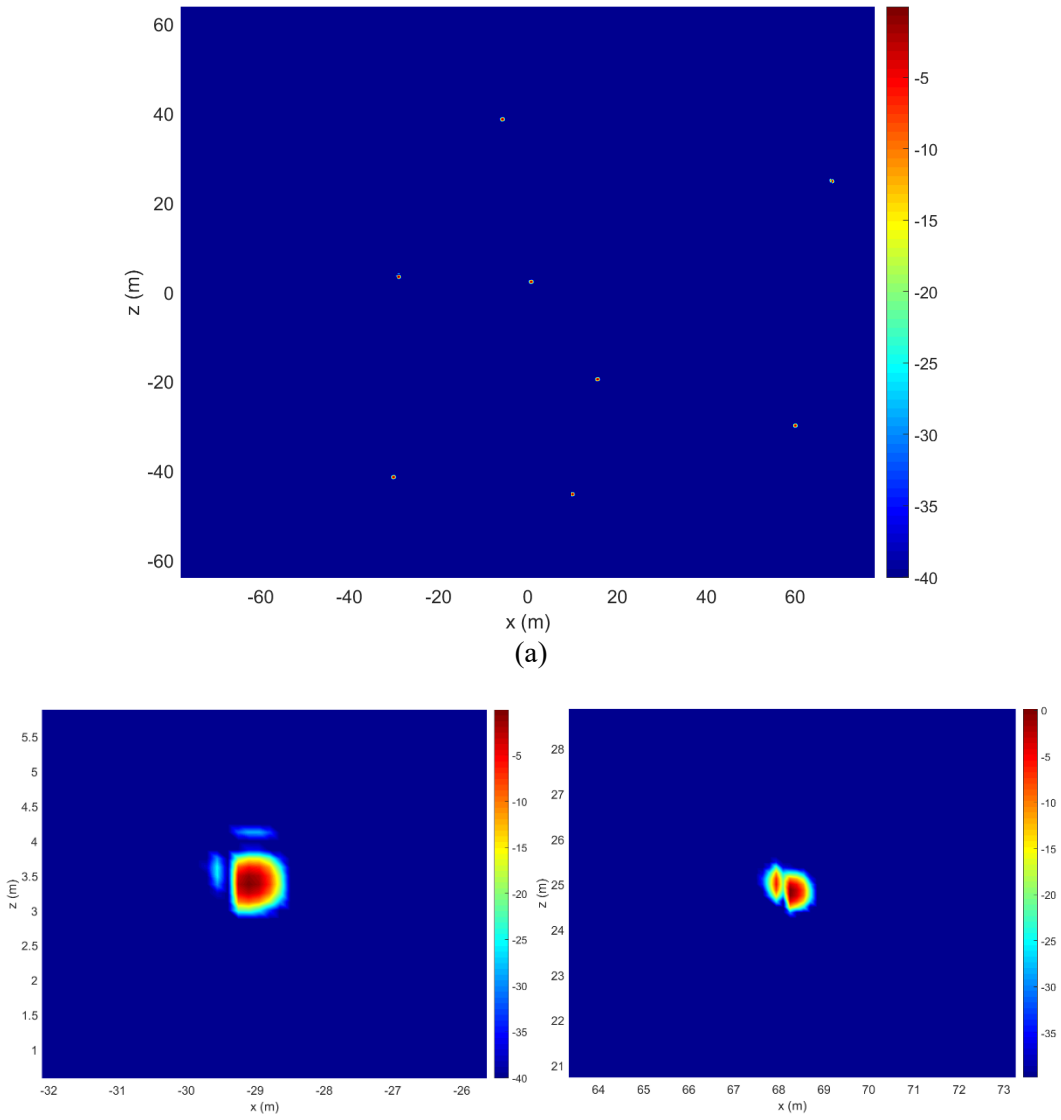

Fig. 12 2-D SAR image obtained by PFA and the WCEC procedure for the forward-looking geometry in the x-z plane for the same point target set as in Fig. 4, showing a) the full image and b) details around two targets exhibiting the split image issue. None of the other target images displays this issue.

Table 4 Target coordinates in the 2-D side-looking and forward-looking SAR configurations, showing the true locations as well as their images obtained by the PFA coupled with the WCEC procedure

Target number	Side-looking				Forward-looking			
	True		PFA with WCEC		True		PFA with WCEC	
	x (m)	y (m)	x (m)	y (m)	x (m)	z (m)	x (m)	z (m)
1	–50.0	60.0	–49.8	60.3	60.0	–30.0	60.4	–29.9
2	52.0	66.5	51.8	66.5	68.2	24.8	68.1	24.8
3	15.6	–6.5	15.6	–6.5	15.6	–19.3	15.7	–19.4
4	10.0	–47.8	9.8	–47.7	10.0	–45.8	10.0	–45.5
5	–29.1	3.6	–29.1	3.6	–29.1	3.6	–29.1	3.4
6	–30.2	–41.4	–30.2	–41.6	–30.2	–41.4	–30.4	–41.4
7	53.3	–50.0	53.4	–49.9	–5.7	38.9	–5.8	38.7
8	–5.7	38.9	–5.8	38.8	0.7	2.3	0.7	2.3

Figure 13 is the corrected image for the full 3-D FLSAR configuration with the uncorrected originally shown in Fig. 5. In this case, the image is broken into 8 × 8 × 4 subimages in the x, y, and z directions, respectively, with each subimage extending over 2.5 × 2.5 × 4 m. In the new, corrected 3-D image, the targets are perfectly focused at the correct locations in the x and y directions, while in the z direction the residual shifts are less than 0.2 m. Note the actual subimage sizes are smaller than the estimates in Eq. 39. From a computational standpoint, a larger number of subimages involves a longer runtime in calculating the WCEC FIR filter coefficients; however, as already discussed, these calculations can be performed offline, outside the main image formation data processing stream. The filtering operation itself is actually faster when we work with a larger number of smaller size subimages. For reference, the filtering part of the WCEC in this numerical example took about 10 s to complete. The only disadvantage of using a large number of subimages is the corresponding large number of discontinuity lines/planes at the subimage boundaries.

4.4 Other Possible Approaches

Besides the WCEC technique described in the previous section, other methods have been developed to mitigate the wavefront curvature errors in PFA. Some of these methods start with the uncorrected PFA image, as does the subimage-oriented WCEC algorithm previously discussed. Other WCEC procedures are embedded directly in the image formation algorithm. In this section, we present a short review of these alternative techniques. We start by describing the former methods, which are related to the procedure in Section 4.3.

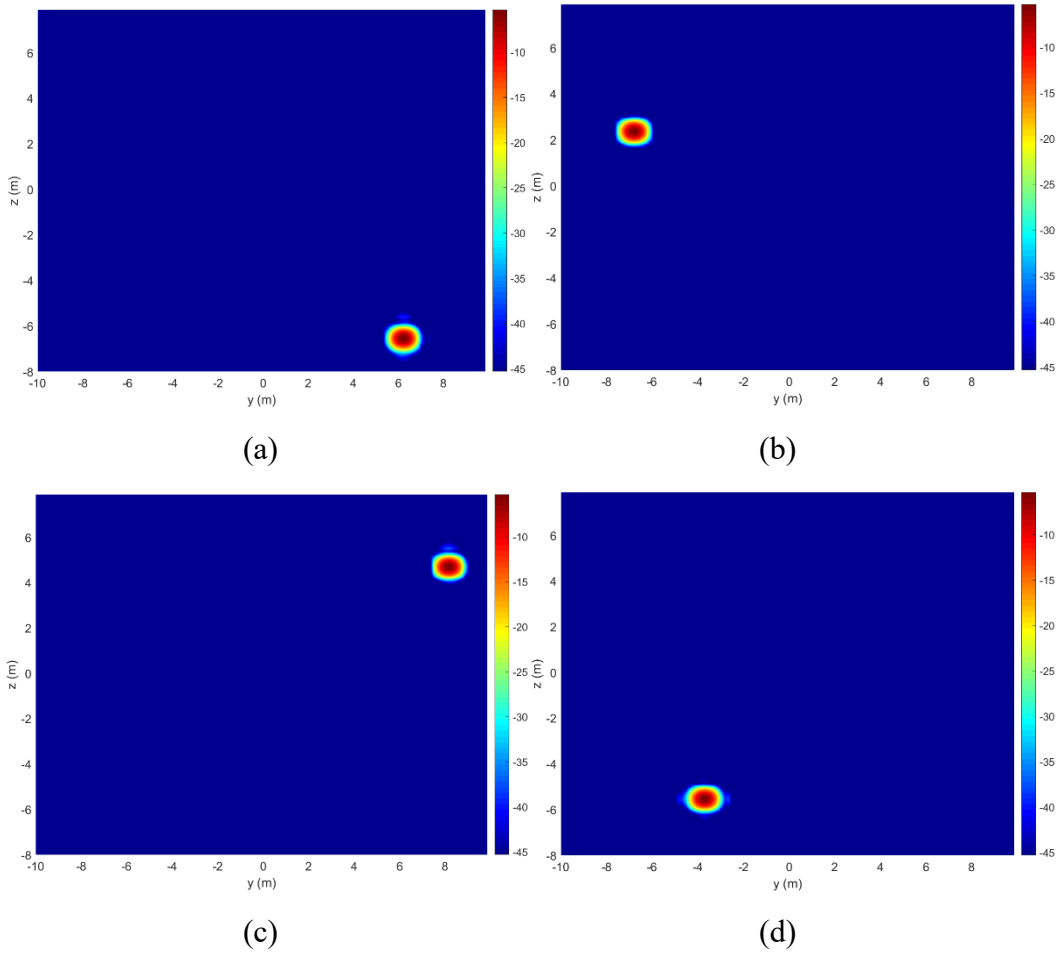

Fig. 13 Vertical y-z planar cuts through the 3-D PFA image obtained for the full FLSAR configuration after the WCEC procedure, at x coordinates corresponding to the four target image peaks: a) x = –8.125 m (Target 3), b) x = –5.937 m (Target 4), c) x = 5.937 m (Target 1), and d) x = 6.719 m (Target 2). The point target true coordinates are listed in Table 2.

One WCEC approach suggested by Carrara[5] only addresses the shifts induced by linear phase errors by computing $\left(a_x, a_y, a_z\right)$ with the formulas in Eqs. 25 and 36, for each pixel/voxel in the image. These shifts are simply used to move the pixels/voxels in the uncorrected image to the new coordinates in the corrected image. Note this approach is applied uniformly across the entire image; no partition into smaller subimages is required, which means this method is not affected by discontinuities at the subimage boundaries. Nevertheless, the problem with this technique is that the formulas in Eqs. 25 and 36 are only approximate, and as discussed in Section 4.1 they can be inaccurate in certain cases. Additionally, the method does not address the quadratic and higher-order phase errors introduced by the wavefront curvature phenomenon.

Better accuracy can be achieved if the shifts $\left(a_x, a_y, a_z\right)$ are instead taken as the coordinates of the peaks characterizing the WCEC filter impulse responses. Since the filter design starts with Eqs. 40 and 41, which are exact, there are no approximations in the shift calculations in this case. However, to eliminate the subimage partition and the related discontinuity issue at boundaries, the filter impulse response (and its peaks) must be computed separately for each image voxel. This seems a formidable computational task, which would likely require an execution time of orders of magnitude longer than any other operations involved in the image formation process. The only way this method could be applied in practice would involve computing the shift coordinates offline and storing them before being applied to the radar data processing stream (note the required amount of storage is insignificant).

An entirely different approach called "subpatch processing"[5] involves breaking the original image domain into smaller pieces (or subimages) and applying the PFA separately for each of these subimages. The subimage size must be limited such that the phase errors characterizing voxels at its edges do not exceed the limits established in Section 4.1. Subsequently, the subimages are assembled (or mosaicked) together into a larger size image. When applying the PFA to a given subimage, we first multiply the radar data by the factor $\exp\left(jk_R r_r\right)$, where the radar range r_r is measured with respect to the center of that subimage. It is clear that this range and the corresponding phase factor $\exp\left(jk_R r_r\right)$ are different for each subimage; otherwise, the PFA proceeds similarly for all subimages.

One important additional step in the subpatch processing approach consists of filtering the radar data to avoid aliasing of targets present in one subimage into all the other adjacent subimages. This anti-alias spatial filtering is similar to the spotlighting procedure described in Section 3.3 and is not detailed here. In the end, the subpatch processing approach to PFA involves a computational complexity similar to the WCEC procedure outlined in Section 4.3. Additionally, the two methods are affected by similar image discontinuity artifacts at the boundaries between subimages.

Finally, another approach to PFA imaging uses subaperture processing[8] to keep the wavefront curvature errors under control. This technique starts with the observation that the wavefront curvature-induced QPE increases with both the image size and the aperture length (see, for instance, Eq. 30). While the subpatch processing approach seeks to minimize the QPE by breaking down the image into subpatches of size below a certain limit, the subaperture processing attempts to achieve the same effect by dividing the total synthetic aperture into segments of smaller lengths. A set of coarse resolution images are created by employing the range-Doppler

approach to SAR imaging,[9] which consists of performing a 2-D FFT of the radar data collected along each subaperture. While these images exhibit low resolution, they are little affected by the wavefront curvature phase errors (see Eqs. 28 and 30, which show that the acceptable error limits increase with the resolution cell size). The set of images obtained for all subapertures are combined together via an FFT in the azimuth (along-track) direction. This process can be broken into several stages ("tiered-subapertures"' in the original reference[8]), each of them involving a number of aperture segments of increasing lengths, until a final image of resolution dictated by the entire aperture length is obtained.

5. Conclusions

This report presents a comprehensive account of the PFA application to the FLSAR system proposed by ARL to assist helicopter landing in DVE conditions. The major motivation for this work has been the development of a fast and accurate image formation algorithm that can handle the challenging 3-D geometry involved in this sensing scenario. In the process, we discovered that many traditional analyses and assumptions associated with PFA for conventional side-looking SAR configurations cannot be directly extended to the forward-looking aperture geometry. Consequently, the original contribution of this report was to reformulate the PFA and the related analysis to make them applicable to the FLSAR imaging system.

After a review of other possible image formation algorithms for this application (such as BPA and RMA), we proposed the PFA due to its speed of execution, relatively simple implementation, and its straightforward data sampling requirements. Numerical examples of PFA for 2-D and 3-D configurations relevant to the FLSAR system were presented in Section 3. Other implementation aspects related to data sampling and interpolation as well as computational complexity were also discussed in the same section. Additionally, we adapted the algorithm to handle the presence of multistatic antenna arrays, which constitute an essential component of the system's hardware.

Although the PFA offers excellent computational efficiency, its major drawback stems from the wavefront curvature phase errors, which produce various image distortions. A detailed analysis of these errors was developed in Section 4, followed by a novel error correction algorithm based on partitioning the SAR image into smaller subimages and applying separate correction filters to each subimage. We described this algorithm implementation in detail, identifying one outstanding issue that is the subject of continuing investigation. Several alternative wavefront curvature error mitigation techniques were briefly reviewed as well.

It was not the purpose of this investigation to develop the fastest possible implementation of this imaging algorithm, whose code was written in MATLAB and run on a regular desktop computer, without the explicit use of parallel processing features. Nevertheless, based on computational complexity analysis, the PFA (including the WCEC procedure) should offer vastly superior execution time as compared with the BPA, which has been the standard image formation algorithm proposed for the FLSAR system so far. At this time it is not clear whether PFA could replace BPA as the image formation algorithm of choice for this project due to the issue of image artifacts introduced by the subimage boundary discontinuities in the WCEC procedure. However, future investigations of this issue may be able to produce an artifact-free imaging procedure.

Even if PFA may eventually prove not to be a practical solution for FLSAR imaging, this report contains some valuable contributions going beyond a particular imaging algorithm:

- An evaluation of the pros and cons of several standard SAR imaging algorithms as applied to the FLSAR system configuration (Sections 2.2, 2.3, and 2.4).
- Sampling criteria for radar and image data generally applicable to all SAR imaging algorithms (Section 3.3). These criteria address both the spatial filtering required to mitigate grating lobes produced by targets outside the image frame and the mitigation of the straddling loss via image pixel oversampling.
- A phase correction procedure that transforms the radar data obtained from a multistatic antenna array into those generated by an equivalent monostatic array (Section 3.5). While this procedure is mandatory in the case of PFA, which is specifically designed to work with monostatic configurations, it can also be applied to other image formation algorithms (BPA or RMA), with benefits in terms of execution speed-up.
- The wavefront curvature phase error analysis in Section 4.1 illustrates a more general approach that can be extended to any type of phase errors characterizing the FLSAR system, including those produced by platform motion. In turn, the motion-induced phase error analysis is a prerequisite to developing motion compensation algorithms, which are regarded as a critical element in this program's success.

6. References

1. Dogaru T. Synthetic aperture radar for helicopter landing in degraded visual environments. Adelphi (MD): Army Research Laboratory (US); 2018 Dec. Report No.: ARL-TR-8595.

2. Kelly C, Dogaru T, Phelan B, Sherbondy K, Narayanan R. Wavefront curvature correction for radar imaging in a degraded visual environment. Proc SPIE. 2020;11408.

3. Nguyen L, Le C. 3-D imaging for millimeter-wave forward-looking synthetic aperture radar (SAR). Proc SPIE. 2020;11408.

4. Dogaru T, Phelan B, Le C, Sullivan A, Wikner D. Development of a forward-looking synthetic aperture Ka-band radar to assist rotorcraft navigation and landing in degraded visual environment. Proceedings of the MSS Tri-Service Radar Symposium; 2020.

5. Carrara W, Goodman R, Majewski R. Spotlight synthetic aperture radar. Norwood (MA): Artech; 1995.

6. Jakowatz C, Wahl D, Eichel P, Ghiglia D, Thompson P. Spotlight-mode synthetic aperture radar: a signal processing approach. Boston (MA): Kluwer Academic Publishers; 1996.

7. Doerry AW. Wavefront curvature limitations and compensation to polar format processing for synthetic aperture radar images. Albuquerque (NM): Sandia National Laboratories; 2006 Jan. Report No.: SAND2007-0046.

8. Doerry AW. Synthetic aperture radar processing with tiered subapertures. Albuquerque (NM): Sandia National Laboratories; 1994 June. Report No.: SAND94-1390.

9. Melvin W, Scheer J. Principles of modern radar–advanced techniques. Edison (NJ): SciTech Publishing; 2013.

10. Soumekh M. Synthetic aperture radar signal processing. New York (NY): Wiley; 1999.

11. Soumekh M. Automatic aircraft landing using interferometric inverse synthetic aperture radar imaging. IEEE Transactions on Image Processing; 1996;5(9):1335–1345.

12. Walker JL. Range-Doppler imaging of rotating objects. IEEE Transactions on Aerospace and Electronic Systems. 1980;16(1):23–52.

13. Richards M, Scheer J, Holm W. Principles of modern radar – basic principles. Raleigh (NC): SciTech Publishing; 2010.

14. Schafer RW, Rabiner LR. A digital signal processing approach to interpolation. Proc IEEE. 1973;61(6):692–702.

15. Oppenheim AV, Schafer RW. Discrete-time signal processing. Englewood Cliffs (NJ): Prentice Hall; 1989.

16. MathWorks web page. Natick (MA): The MathWorks Inc.; 2020 [accessed 2020 Sep]. http://www.mathworks.com/products/matlab/.

17. Press WH, Vetterling WT, Teukolsky SA, Flannery BP. Numerical recipes in Fortran 77. Cambridge (UK): Cambridge University Press; 1992.

18. Phelan B, Ranney K, Gallagher K, Clark J, Sherbondy K, Narayanan R. Design of ultra-wideband (UWB) stepped-frequency radar (SFR) for imaging of obscured targets. IEEE Sensors Journal. 2017;17(14).

19. Lim JS. Two-dimensional signal and image processing. Upper Saddle River (NJ): Prentice Hall; 1990.

List of Symbols, Abbreviations, and Acronyms

1-D	one-dimensional
2-D	two-dimensional
3-D	three-dimensional
ARL	Army Research Laboratory
BPA	backprojection algorithm
CCDC	US Army Combat Capabilities Development Command
DVE	degraded visual environment
FFT	fast Fourier transform
FIR	finite impulse response
FLSAR	forward-looking synthetic aperture radar
LFM	linear frequency modulation
MMW	millimeter wave
PFA	polar format algorithm
PSF	point spread function
PSP	principle of stationary phase
PTR	point target response
QPE	quadratic phase error
RMA	range migration algorithm
RVP	residual video phase
Rx	receiver
SAR	synthetic aperture radar
Tx	transmitter
WCEC	wavefront curvature error correction

1 (PDF) DEFENSE TECHNICAL INFORMATION CTR DTIC OCA

1 (PDF) CCDC ARL FCDD RLD DCI TECH LIB

6 (PDF) CCDC ARL FCDD RLS RM A SULLIVAN T DOGARU C LE B PHELAN FCDD RLS RE K RANNEY FCDD RLS RR D WIKNER